Solar line filling on Venus is consistent with broad sunlight induced fluorescence

Jan Spacek
Full report and calculations accompanying the executive summary
25 September 2026

Abstract

The strong absorption inferred for the liquid in Venus's clouds gives a reason to look for fluorescent organic material. Sunlight-induced fluorescence can be sought through the filling of solar absorption lines, as it is over vegetation and ocean plankton on Earth. Public Venus spectra were examined with this method. The work began with CFHT/ESPaDOnS and was extended to VLT/ESPRESSO, VLT/UVES and Hubble/STIS. Positive apparent line filling survives several changes of reference spectrum, sky treatment, extraction, masks and line width. Direct comparison of 33 ESPRESSO exposures with Vesta gives a median green line-depth dilution of 6.24%, equivalent to added light equal to 6.66% of the reflected continuum under the fitted model. UVES and STIS also give positive green coefficients, although their sampled clouds and instrumental responses differ. A simple CO_2 rotational Raman spectrum does not explain the larger CFHT offsets. Complete Raman transport and broad instrumental redistribution remain unresolved. Later checks weaken the original claims of negligible violet filling and large short-term variation. The UV-color association changes sign between scans; no spatially matched UV correlation was obtained. A normalized added-light spectrum is reconstructed under an assumed continuum calibration and compared with the 2026 absorption model. The observations are consistent with broad fluorescence. No tested alternative has been established as a complete explanation with independently measured parameters. The observations justify further fluorescence measurements and a search for absorption-linked circular polarization. The calculations, rejected cases and earlier reconstructions are retained so that this interpretation can be checked.

Contents

1 Why the search was made 3

2 What is measured by line filling 3

3 The original CFHT observations 6

4 ESPRESSO: a direct comparison with Vesta 9

5 UVES: a reduction from raw observations 13

6 Hubble/STIS: a check above Earth's atmosphere 17

7 A conditional reconstruction of the added-light spectrum 21

8 Can other processes produce the line filling? 23

9 Comparison with fluorescence on Earth 29

10 Should fluorescence follow the UV-dark clouds? 31

11 Tests that would decide more 34

12 Conclusion 36

Appendix A. The named solar-line neighborhoods 37

Appendix B. The sixteen earlier CFHT reconstructions 38

Appendix C. Worked calculations 42

Acknowledgments and use of AI 44

References 45

The main text is followed by the full named-line catalog, the sixteen earlier CFHT reconstructions, worked calculations, and a guide to the data attachment.

1 Why the search was made

Our 2026 paper began with a familiar problem: something in Venus's clouds absorbs strongly in the ultraviolet and blue. Under the adopted cloud model, very strong absorption is required inside the liquid droplets. The modeled decadic absorption coefficient reaches about 1,278 cm^{-1} at 375 nm. Efficient conjugated organic molecules could provide that absorption at high concentrations (Spacek et al. 2026).

That result suggested a further test. If much of the absorption is supplied by organized organic carbon, some absorbed sunlight might be returned as fluorescence. Here, organized carbon means carbon joined into light-absorbing molecular structures, including conjugated systems. Cells and biological organization have not been identified by the absorption model. A porphyrinoid is one candidate class, but no particular molecule is assumed in the spectral fits.

Fluorescence follows electronic excitation. A molecule absorbs a photon and is raised to a higher energy state. Some of that energy can subsequently leave as another photon, usually at a longer wavelength. Much can also be lost as heat or through chemical reactions. Acidity, protonation, metals, aggregation and concentration can change or suppress emission. Thus strong organic absorption supplies a reason to search for fluorescence, not a guaranteed brightness. Experiments with organic chemistry in concentrated sulfuric acid provide a relevant laboratory setting, but their products have not been identified in Venus's clouds (Spacek et al. 2024).

The practical example was supplied by Earth. Chlorophyll fluorescence is retrieved remotely from solar absorption lines over land and water (Joiner et al. 2011; Wolanin et al. 2015; Köhler et al. 2020). This sunlight-induced fluorescence is often called SIF. Its measurement shows how a weak emission can be recovered from much brighter reflected sunlight. The same optical method can be applied to Venus without assuming that the emitter is chlorophyll.

I first asked whether the available Venus spectra contained the expected line filling, with a broad enhancement near the green and less filling toward 400 nm. That proposed shape was tested. It was not required by the fits. The later empirical-reference comparisons were particularly useful because they changed part of the initial picture: appreciable violet filling remains, and a sharp maximum at 500 nm is not established by the line-depth coefficients alone.

This report brings together the calculations made during that search. The line measurements are newly calculated from public observations; they are not previously published fluorescence detections. The observational programs deserve credit for the spectra. The interpretation presented here remains open to independent review.

2 What is measured by line filling

Solar lines and added light

Dark Fraunhofer lines are formed in the Sun before sunlight reaches Venus. Ordinary reflection carries those lines into the planetary spectrum. A smooth emission adds photons inside the lines as well as between them. The line depths are reduced after the observed spectrum is normalized to its own continuum.

Let S be a solar profile normalized to a continuum of one, C the reflected continuum, and F a locally smooth addition. Then

$$I = C\,S + F; \quad f = F/C; \quad I/(C + F) = (S + f)/(1 + f). \quad (1)$$

The fractional reduction of the original line depth is

$$q = f/(1 + f); \quad f = q/(1 - q); \quad D_{observed} = (1 - q)\,D_{solar}. \quad (2)$$

The distinction between f and q is kept throughout the report. A value f = 10% means q = 9.09%. If the original normalized line is 70% deep, its depth is reduced by 6.36 percentage points of the total continuum. It does not become ten percentage points shallower. Under the same smooth-continuum assumptions, the equivalent width is reduced by q. Ordinary convolution conserves the area of an isolated line when the full profile is integrated with a correct continuum; a restricted window or broad scattered wings can hide that distinction.

Neither coefficient is a fluorescence quantum yield. The yield is the number of emitted photons divided by the number of absorbed excitation photons. Absolute radiance, an excitation spectrum and a cloud-transport model would be needed to infer it. Positive f or q is described here as apparent added light or line dilution until its cause is established.

Local spectral models

For the original CFHT analysis, four-nanometer neighborhoods were fitted with

$$I(\lambda) = P_2(\lambda)\, S_{Venus}(\lambda) + Q_1(\lambda)\, S_{sky}(\lambda) + d. \quad (3)$$

P_2 is a quadratic reflected continuum and Q_1 is a linear sky continuum. Both solar templates share one fitted Gaussian width in that implementation. Separate velocity shifts distinguish Venus light from terrestrial scattered sunlight. In one 2018 treatment, the measured simultaneous sky spectrum replaces the second solar template. The reported coefficient is d/P_2 at the center of the window. Signed coefficients are retained. A negative coefficient is a model diagnostic, not negative physical emission.

The ESPRESSO primary model uses P_2 times a shifted and broadened solar reference plus d. Its final empirical comparison uses a resolution-matched Vesta spectrum as the reference. UVES and STIS use the equivalent normalized form $P(\lambda)[(1 - q)S(\lambda) + q]$, with their stated continuum and instrumental profiles. In the UVES sky-control model, an additional fractional solar-sky term k is included. The Venus-only ratio is then $f = q/(1 - q - k)$, not $q/(1 - q)$.

The IAG disk-integrated solar atlas supplies the main reference below the telluric-clean atlas boundary. The Baker atlas is used above about 501 nm, where available (Reiners et al. 2016; Baker et al. 2020). "Telluric" means absorption in Earth's atmosphere. Even a space-based Venus spectrum can be biased by telluric features left in a ground-based solar reference.

Wavelength conventions were checked separately for each instrument. CFHT neighborhoods and the named-line catalog are given in air wavelengths. ESPRESSO fits use vacuum wavelengths in the archive barycentric frame. UVES air wavelengths are converted once to vacuum, and its residual velocity is fitted without imposing an unverified barycentric correction. STIS uses a custom initial dispersion solution and a fitted local offset. A wavelength label in one frame must not be compared directly with a line center in another.

Selection and uncertainty

Bad pixels, strongly contaminated terrestrial bands and unsuccessful fits were excluded by the stated rules. Where residual clipping was used, it was symmetric. Negative additions were not removed merely because they disagreed with fluorescence. No Gaussian emission band was imposed on the fitting coefficients.

Neighboring wavelength windows, spatial rows and repeated visits are correlated. Coadded products and their constituent exposures also contain the same photons. Their counts must not be added as independent detections. Least-squares errors in the tables are conditional on the reference, extraction, continuum and instrumental model. They do not include every systematic uncertainty. Exposure ranges and spatial spreads are therefore reported as sample descriptions, without assigning a formal significance to fluorescence.

The saved analysis stages are summarized in Table 1. The original pilot and denser CFHT sample share 55 Venus products, leaving 193 unique products across those two stages. The sky audit and reconstruction reuse observations from the broader work. No grand total of independent detections is inferred from the number of fitted windows.

Table 1. Data used in the analysis. Counts describe the specified stage; overlapping stages are not additive.

Stage	Observations or fits	Principal use
CFHT pilot	54 Venus spectra in six campaigns, nine airless controls, then three 2018 Venus spectra	Initial survey and reference checks
CFHT denser scans	191 Venus products; 4,573 returned fits from 4,584 attempted windows	Time and UV-color comparisons
CFHT sky audit	42 Venus observations; 420 sky fits and 1,008 target refits	Contamination of the nominal sky aperture
CFHT alternative models	Five Venus spectra, Moon, Ceres and Jupiter; 1,848 local fits	Raman shapes and instrumental wings
CFHT reconstruction	16 exposures, 873 accepted windows	Earlier conditional emission shapes
Jupiter	One CFHT spectrum, 21 May 2005	A comparison with a planet known to show Raman filling
ESPRESSO	33 individual Venus exposures; 17 primary products, mostly coadds; ten reflector controls	Independent detection and empirical Vesta reference
UVES	Ten bright frames and one faint diagnostic from 194 inventoried Venus frames	Raw reduction, spatial rows and extraction checks
Hubble STIS	Two exposures on 27 January 2011; 16 retained green spatial bins in total	Independent measurement above Earth's atmosphere

3 The original CFHT observations

Profiles and the campaign survey

The CFHT observations were made with ESPaDOnS and retrieved from the Canadian Astronomy Data Centre. The archived Upena/Libre-ESpRIT extractions were used (Donati et al. 1997). These spectra sample parts of the disk; they are not disk-integrated Venus measurements. Some were obtained for cloud-wind studies, in which Doppler shifts of the same solar lines were measured (Machado et al. 2021).

The initial query returned 3,545 reduced Venus products under the names searched. That is an archive inventory, not an exhaustive census. Three neighboring exposures were selected near each of three chronological percentiles in six campaigns, giving 54 pilot spectra. Three 2018 star-plus-sky observations brought the pilot to 57. Nominal resolving powers were about 80,000 and 65,000 for the principal modes. Forty-seven of the first 54 Venus exposures passed the main sky cut.

Several actual line neighborhoods are shown in Figure 1. The matched reflection profile is shallower after a positive smooth component is included. In this figure, the reflection-only profile shares the shift and width of the additive fit; it is a visual comparison, not a separately optimized zero-addition hypothesis. The coefficients were fitted over four nanometers, wider than the displayed cores.

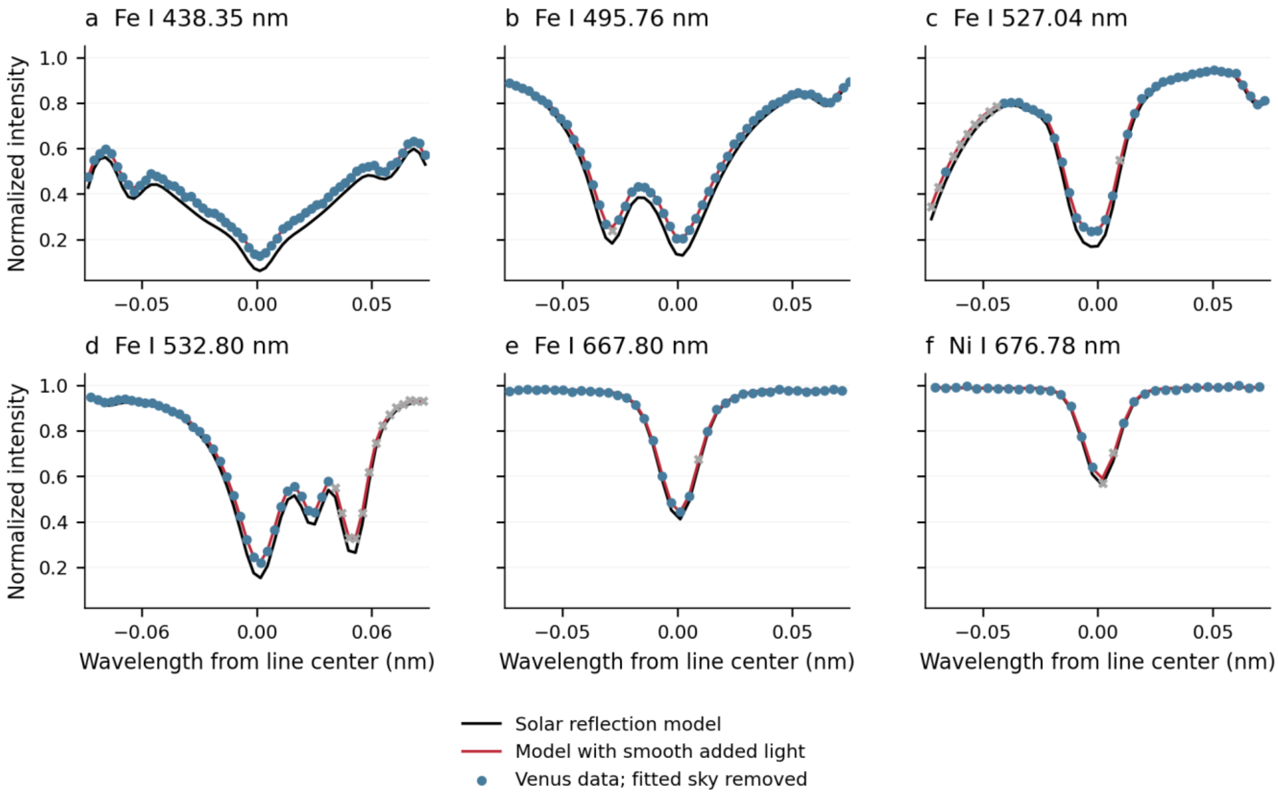

Figure 1. CFHT Venus exposure 2298946i, observed on 22 August 2018. Blue points are retained data after fitted sky subtraction; gray crosses mark excluded samples. The matched reflected solar profile is black and the model with a smooth addition is red. Each panel displays part of a four-nanometer fit. The panels are examples of a shared line-depth discrepancy, not six independent detections of fluorescence.

Representative green f values range from about 4.3% to 13.0%. The original campaign medians were approximately 5.4% in 2007, 5.7% in 2009, 11.5% in 2011, 12.0% in 2014, 12.3% in 2015 and 13.0% in 2016. These values combine different geometries and observing conditions. They do not establish a secular change in emission from Venus.

The three 2018 measured-sky fits gave green f of about 9.7%, 9.2% and 11.0%. For 2298946i, comparison with a smoothed Ceres reference lowered green f from about 9.7% to 8.2%. The empirical comparison retained about 4.1% near 400 nm and 5.4% over 625–685 nm. Airless controls generally retained roughly 1% apparent green filling, with negative values possible in the violet. Reference choice therefore affects both the zero level and the inferred spectral shape.

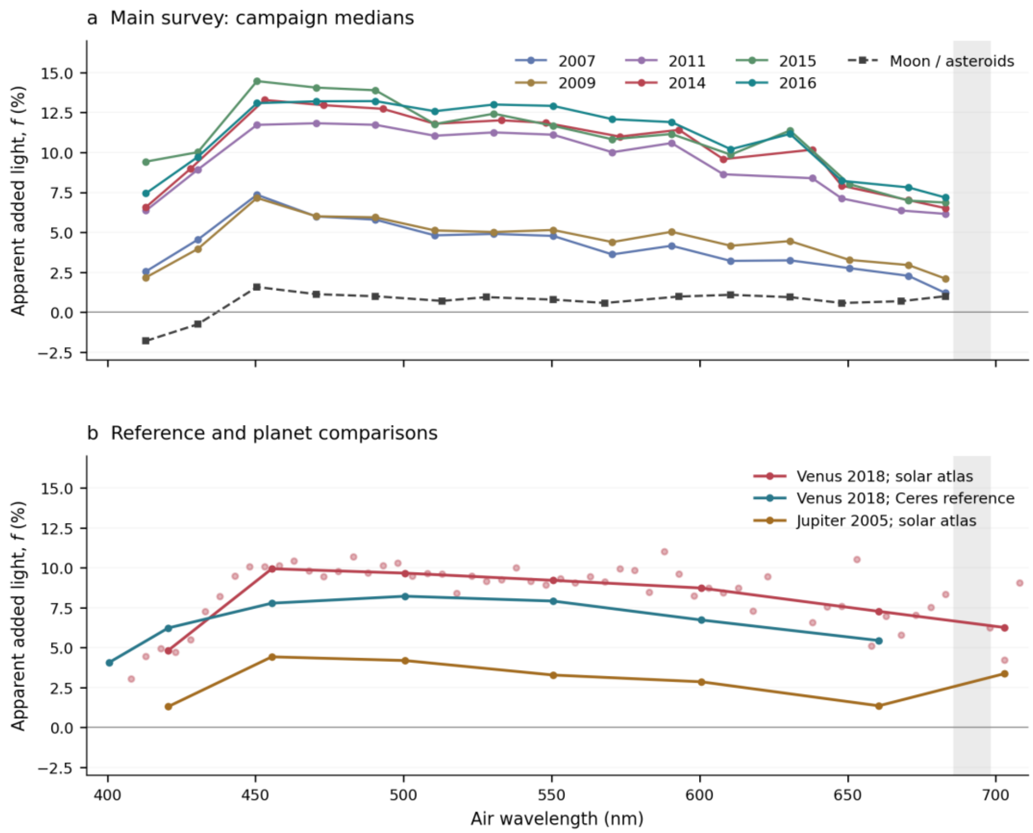

Figure 2. Original CFHT survey and reference checks. The campaign curves summarize f in 20 nm bins after the stated cuts. The comparison panel shows individual Venus/atlas windows and binned medians for Venus/atlas, its empirical Ceres check and Jupiter. The gray 686–698 nm interval is strongly affected by terrestrial oxygen. These are line-filling coefficients, not emission-energy spectra. The later ESPRESSO reference test in Figure 3 limits the interpretation of the violet-to-green contrast.

Changing between normalized and unnormalized extractions changed the green median by less than 0.08 percentage points in six checked spectra. An alternative terrestrial mask changed the representative 2018 value from 9.66% to 9.76%; the April 2014 example remained at 12.81%. Two checked Venus raw frames contained no saturated pixels and peaked at 29,927 and 18,370 ADU, below their header saturation level of 65,535 ADU. This check does not establish the full detector response. The checked Ceres raw frame contained 23 saturated pixels; their relevance to the fitted orders was not established.

Known artificial additions were also recovered. Gaussian additions centered at 500 nm, with width σ = 50 nm and peaks of 0.1%, 1% and 5%, were injected into observed spectra. In windows where the added signal exceeded 10% of its peak, the median recovery ratio was 1.001. This verifies the calculation's response to an imposed smooth addition. It does not determine the cause of the original offset or a complete detection threshold.

Jupiter as a positive comparison

The single Jupiter spectrum, 794257i, was taken on 21 May 2005 with a 300 s integration, airmass 1.08 and the Sun about 28.6° below the horizon. Green f is 4.19% against the solar atlas and 2.97% or 2.55% against empirical Moon and Ceres references. Normalized versus unnormalized extraction changes the green result by less than 0.01 percentage points.

This is qualitatively consistent with known filling of Jovian solar lines by molecular-hydrogen Raman scattering. Cochran et al. (1981) detected that process in spectra covering 385–503 nm and identified shifted solar structure associated with the H_2 rotational transitions. Recovering line filling in this known case supports the method's ability to detect the effect. No hydrogen Raman transport fit was performed here, so the present f values are not a quantitative validation of that mechanism. Jupiter's atmosphere, cloud paths and rotational broadening differ from Venus's; its coefficient cannot be subtracted as a Venus baseline.

4 ESPRESSO: a direct comparison with Vesta

Observations and fitted windows

The ESPRESSO archive supplied an independent set of high-resolution spectra. The Venus observations were made on 2–3 September 2018 in the ultra-high-resolution mode on VLT Unit Telescope 3, with a nominal resolving power of 190,000 and a 0.5 arcsecond aperture. Seventeen primary products contained 33 distinct exposures: sixteen pairs and one single exposure. Their total exposure time was 162 seconds. The dates in the 2021 archive product names refer to processing; they are not observing dates.

The primary analysis uses the original extracted electrons from fibre A. The coadds were checked, but their photons were not counted again as independent observations. Four-nanometer windows were fitted at five-nanometer intervals from 408 to 713 vacuum nm. A local quadratic continuum, velocity, Gaussian width and additive component were fitted. The primary A analysis returned 1,717 accepted windows. None reached the fitted width or velocity bounds. The median normalized residual RMS was 0.414%.

Ten observations of reflecting bodies were also examined: eight Vesta products, one Ceres and one Ganymede. The most useful comparison was a Vesta observation made on 19 November 2018 in the same ultra-high-resolution mode. The reference and Venus spectra were smoothed by Gaussian velocity dispersions of 2.9 and 3.0 km s^{-1}, respectively, before fitting a further width. This step reduced sensitivity to a small difference in their narrow instrumental cores. The direct Venus/Vesta calculation returned 1,716 accepted fits.

The green result changes little when Vesta replaces the solar atlas. The violet result changes substantially. Against the atlas, the UHR Vesta controls themselves have negative violet coefficients. Direct comparison with Vesta therefore raises the inferred Venus violet filling. The original expectation of almost no filling near 400 nm is not supported by this control. These data begin near 406 nm; they do not measure exactly 400 nm.

Table 2. ESPRESSO band summaries. Each value is the median of the exposure medians. All bands are in vacuum nm. The range is the full range among 33 exposures, not a confidence interval. The final column is the separately summarized f coefficient.

Reference	Band, nm	Median q, %	Exposure range, %	Median f, %
Solar atlas	406–435	2.77	2.35–3.77	2.85
Solar atlas	475–525	6.45	6.26–7.60	6.89
Solar atlas	540–585	6.23	5.93–7.32	6.65
Solar atlas	650–715	4.45	3.84–5.27	4.66
Vesta	406–435	5.34	4.98–6.33	5.64
Vesta	475–525	6.24	6.07–7.35	6.66

Reference	Band, nm	Median q, %	Exposure range, %	Median f, %
Vesta	540–585	6.35	6.14–7.52	6.79
Vesta	650–715	4.03	3.44–4.82	4.20

Figure 3. ESPRESSO line dilution from the solar atlas and the empirical Vesta reference. The accepted window and exposure summaries are shown with the saved control spectra. The green addition remains near 6% of the total continuum. Vesta changes the violet zero level. The plotted variation describes the observed sample and fitting choices; it is not an uncertainty envelope for a physical fluorescence spectrum.

The second fibre contains Venus light

The sky-subtracted archive column initially appeared to show a large change between the two nights. That interpretation failed a velocity check. The removed component has a velocity of about −33.5 km s^{-1}, matching Venus and differing from terrestrial scattered sunlight near −20.7 km s^{-1}. The effective removed signal is about two thirds of fibre A in the green. Its precise route into the second fibre was not reconstructed, but it cannot be treated as blank terrestrial sky.

The nightly A/atlas green medians are 6.42% and 6.45%. After the pipeline subtraction they become 4.60% and 2.89%. The direct A/Vesta values are 6.13% and 6.25%. Thus most of the large night-to-night contrast in the subtracted column was introduced by removing a Venus-bearing spectrum. This contrast cannot be used to reject a fixed instrumental cause or to establish variable fluorescence.

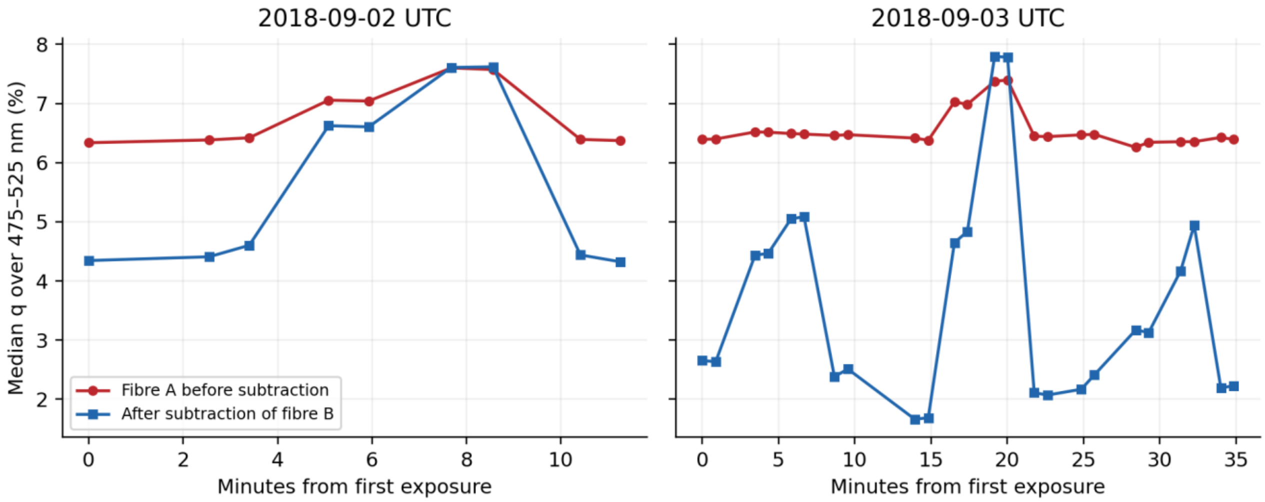

Figure 4. The original fibre-A spectra and the corresponding A−B products are compared by exposure and night. The component removed by the matched extracted-electron subtraction carries Venus's Doppler shift. This check changes the interpretation of the apparent temporal signal. The preferred measurement uses A before that subtraction.

A second solar template at terrestrial velocity was also added to the A model. Its fitted coefficient was small, about −0.31% to +0.34% of the reflected continuum in the selected tests. The green q changed by −0.11 to +0.23 percentage points. Ordinary terrestrial sky leakage in those tests did not supply the main green addition.

Profile and numerical checks

Changing the continuum degree from one to three and the window width from two to six nanometers left representative green q between 6.523% and 6.755%. Using the Reiners atlas alone changed the green coefficients by a median of 0.007 percentage points and at most 0.205 points. A known 5% continuum-fraction injection was recovered at 96.6–100.9% of its input, with a median recovery of 100.02%. These tests check the calculation under its assumed model. They do not determine the true instrumental scattering profile.

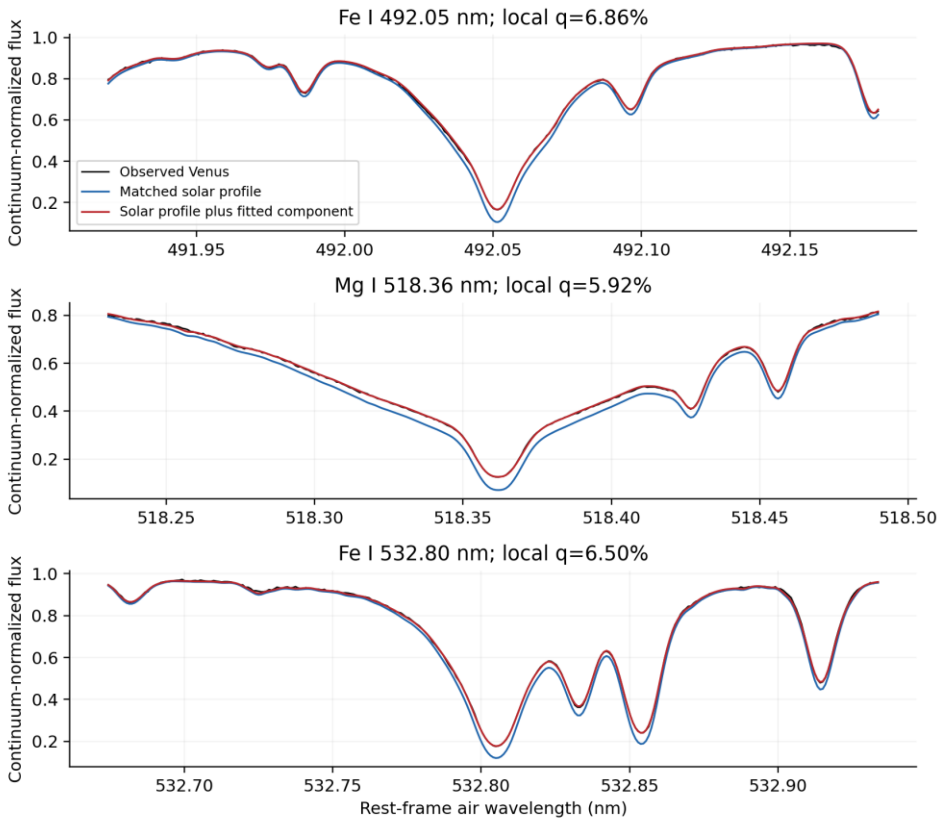

Figure 5. Actual ESPRESSO line neighborhoods fitted against the solar atlas; the displayed q values use that reference, not Vesta. The reflection-only illustration uses the shift and width from the additive fit. It shows how the inferred smooth component changes the line depths; it is not an independently reoptimized null model. The full fitting windows, masks, coefficients and residuals are retained in the accompanying tables.

Broad instrumental wings were tested separately. Positive Gaussian halos with dispersions of 20–100 km s^{-1} fitted the selected windows less well than a smooth addition. A much broader 300 km s^{-1} halo could approach the fit quality with about 8.7–9.1% of the profile area. Such a halo was not measured in ESPRESSO. It demonstrates why an independently calibrated response to an extended bright source is still needed. Vesta is a compact source observed later, so it does not by itself calibrate every difference in illumination by Venus.

5 UVES: a reduction from raw observations

Selection, calibration and slit rows

The UVES program inventory contains 194 Venus frames and 24 comparison-star frames from August–September 2018. Eleven Venus frames were reduced for this analysis. Ten bright frames form the main sample: six RED580 frames, three on each of 29 August and 3 September, and four BLUE437 frames, the first and last selected exposure on each night. A faint RED580 exposure from 20 August was retained as a diagnostic. The full campaign was not reduced.

The raw science and associated calibration files were processed with UVES pipeline 6.1.8 and EsoRex 3.13.7. Two-dimensional extraction was retained. Interorder background was subtracted, but no strip of the Venus slit was declared blank sky and subtracted from the planet. The RED bias was rebuilt from the same five calibration progenitors with trap interpolation disabled after that correction produced an artifact.

The BLUE slit was 0.3 by 10 arcseconds and covered about 373.21–499.98 air nm. The RED slit was 0.3 by 12 arcseconds and covered 472.64–683.50 air nm across its two chips. Each air wavelength axis was converted once to vacuum. The velocity was then fitted. Its value near −13 km s^{-1} is topocentric and is consistent with the ESPRESSO frame after accounting for the latter's barycentric correction.

Individual slit rows were fitted separately. Adding rows before aligning their spectra would broaden the lines through slit tilt and could imitate filling. The typical fitted Gaussian dispersion was about 1–1.6 km s^{-1}. In the main RED measurements, a linear continuum and q were fitted. The sky and continuum controls used more flexible models.

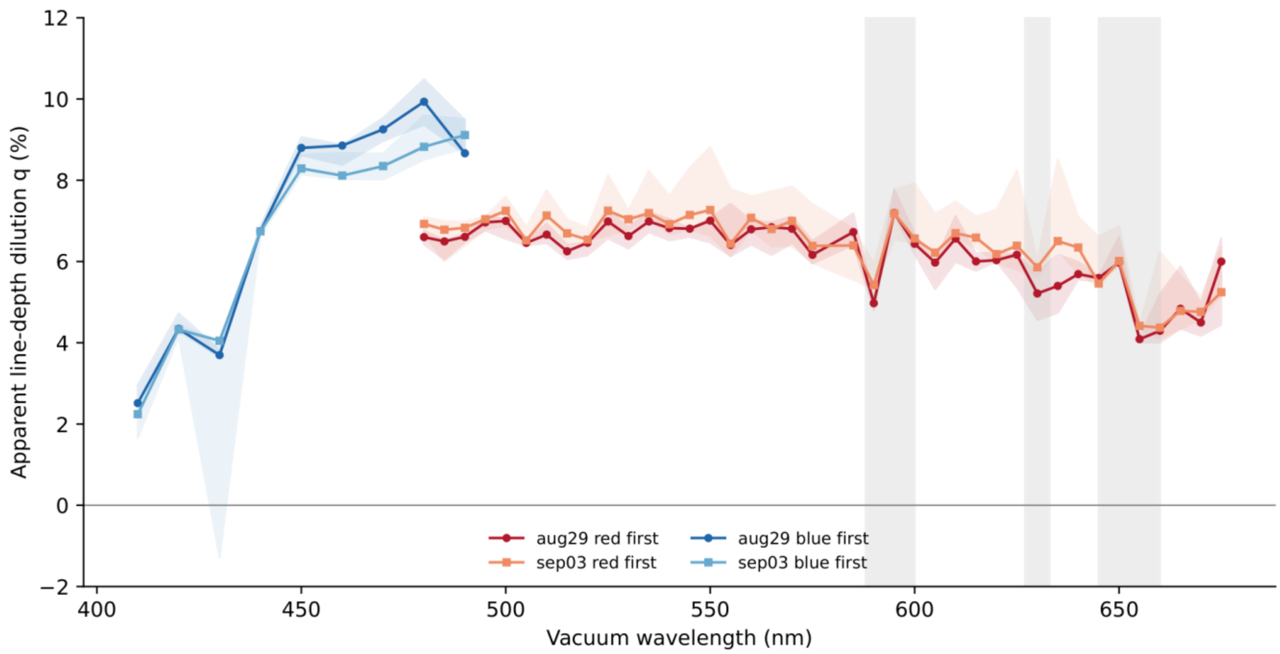

Figure 6. UVES line dilution in the selected BLUE437 and RED580 observations. Each point is the median of three separately fitted rows; shading spans their minimum–maximum. The gray wavelength intervals flag regions sensitive to terrestrial absorption or broad-line continuum placement. BLUE and RED were observed at different times and positions; their coefficients have not been joined into a single calibrated emission spectrum.

Table 3. UVES green-window results. RED combines centers at 480, 490, 500, 510 and 520 vacuum nm; BLUE combines 480 and 490 nm. Three separately fitted rows are represented in each exposure. The spread is the 16th–84th percentile across row/window combinations, not an error on an independent mean.

Date and exposure	Arm	Median q, %	Sample spread, %	Median f, %
29 Aug, first	RED	6.60	6.46–6.90	7.07
29 Aug, second	RED	6.33	6.20–6.61	6.76
29 Aug, third	RED	7.02	6.49–7.39	7.55
3 Sep, first	RED	6.88	6.57–7.22	7.39
3 Sep, second	RED	6.00	5.76–6.21	6.39
3 Sep, third	RED	7.22	6.72–7.46	7.79

Date and exposure	Arm	Median q, %	Sample spread, %	Median f, %
29 Aug, first	BLUE	9.43	8.66–10.05	10.41
29 Aug, last	BLUE	8.51	7.87–9.14	9.30
3 Sep, first	BLUE	8.97	8.73–9.52	9.85
3 Sep, last	BLUE	9.12	9.09–9.23	10.04

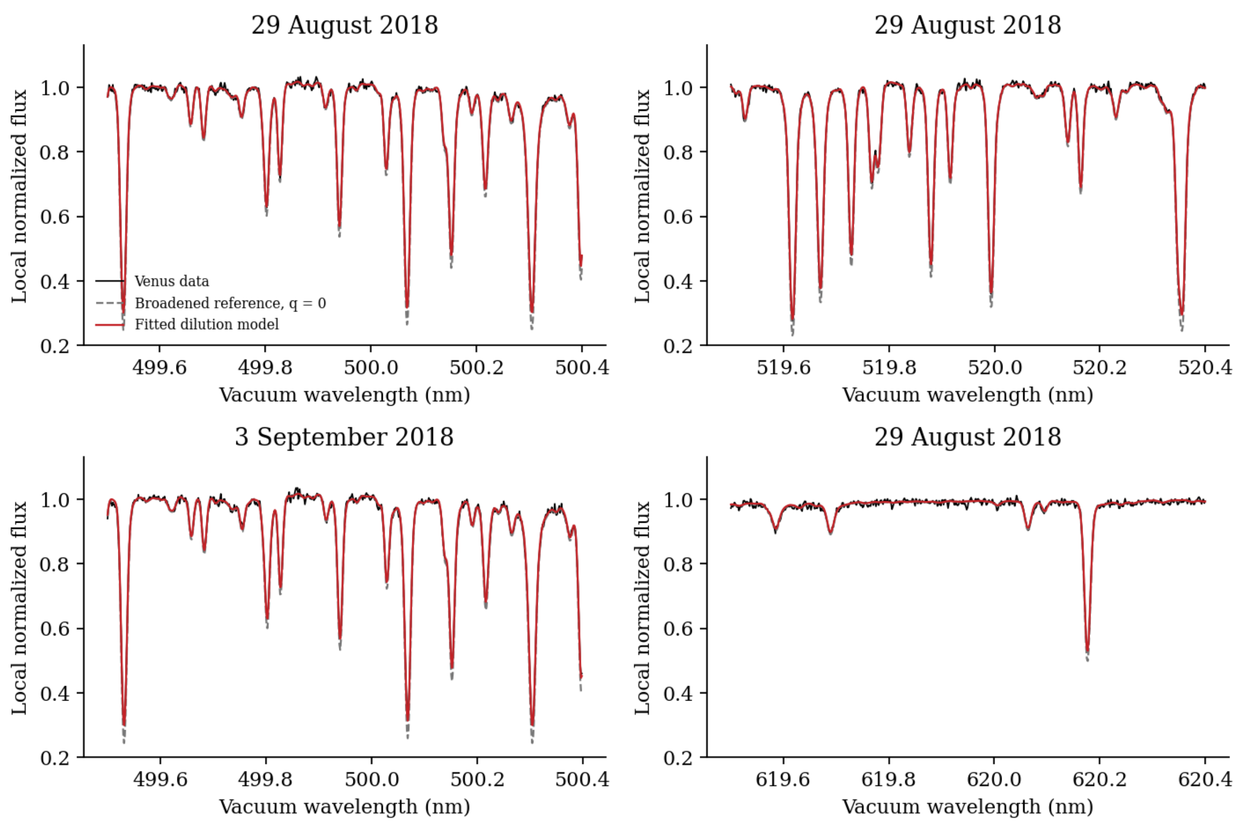

Figure 7. Representative UVES spectral neighborhoods from the raw-data reduction. The q = 0 illustration shares the nuisance parameters of the additive fit. Positive coefficients occur in several solar-line groups. They are fitted over neighborhoods, not measured as flux in one isolated atomic transition.

What the reduction tests changed

Disabling the RED bias trap correction changed selected green q by at most 0.012 percentage points. It removed a documented reduction artifact without removing the broad green discrepancy. A two-component line-spread function, with 20% of its area in a component three times wider than the core, lowered RED q by a median of 0.45 points and at most 0.85 points. BLUE changed by up to 1.25 points. This particular wing model did not account for the full signal.

The RED quadratic-continuum and second-solar-template controls changed q by at most 0.57 points. The Reiners-only reference changed it by at most 0.34 points. Substitution of the ESPRESSO Vesta reference changed RED q by at most 0.40 points and retained a green value near 6.6%. Vesta here tests the solar reference; it is not a UVES instrumental standard. At 410 nm the BLUE coefficient rose from about 2.5% to 6.4% with that reference. This again prevents a firm claim of a nearly empty violet endpoint.

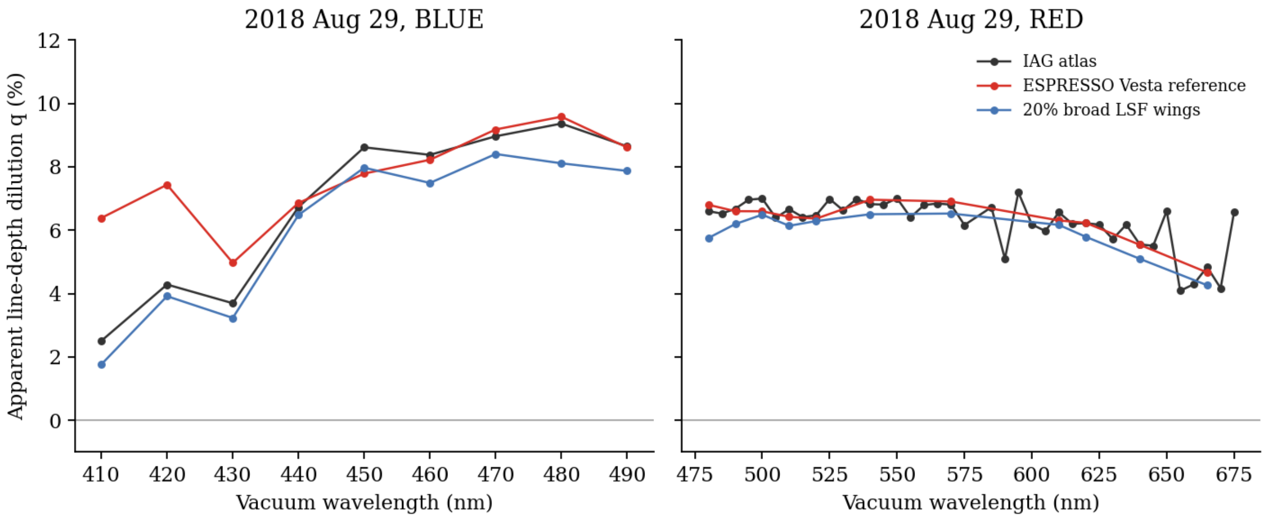

Figure 8. UVES comparisons using IAG, Vesta and the tested instrumental-wing profile. The positive RED green result remains after these changes. The larger violet reference shift and the difference between BLUE and RED show why a complete calibrated shape cannot be inferred simply by connecting all coefficients. The sky and continuum controls described in the text are separate calculations.

The BLUE pipeline error arrays required a separate investigation. Multiplying a master flat by 1,000 left the pre-merge science flux unchanged but changed the propagated relative errors from a median of 9.50% to 0.524%. The resulting order weights changed some merged fluxes. The median absolute change was 0.058%, with 95th and 99th percentiles of 1.28% and 2.05%; about 9% of samples between 420 and 480 nm changed by more than 1%. This scaling was used as a diagnostic, not adopted as a new physical flat calibration. Formal errors derived from those arrays cannot be treated as an absolute detection significance.

Uniform fitting weights altered representative BLUE q by up to 0.84 points. Since that test does not undo an earlier weighted merge, a further calculation was made from unmerged calibrated orders. For row 19 on 29 August, central order pixels gave q = 9.25% at 480 nm and 8.70% at 490 nm. Masking within 0.5 nm of the joins gave 9.43% and 9.16%. Across the nine tested windows, the largest difference from the unweighted pipeline-merged fits was 0.90 points, or 1.36 points with the join masks. Positive BLUE filling remains in this row. The test does not certify every BLUE frame or its uncertainty array.

The four BLUE raw maxima were 21,926–48,717 ADU, below 50,000. The RED 99.9th-percentile levels were about 19,000–29,000 ADU. Sparse high outliers were present, including eight pixels above 65,000 in the third 29 August frame. Widespread continuum clipping was not found, and the first positive 3 September frame had no pixel above 50,000. Detector nonlinearity below saturation was not independently calibrated.

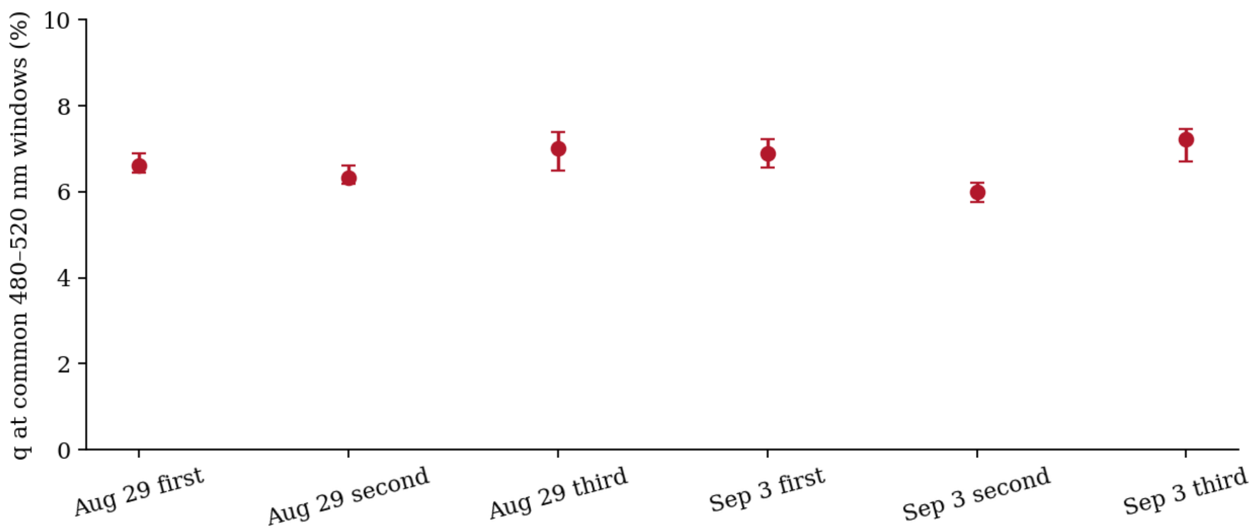

Figure 9. Green-window medians for the six selected UVES RED580 exposures, three on each night. Bars span the 16th–84th percentiles across the separately fitted rows and common 480–520 nm windows. Positive green filling is repeated. Changes among exposures cannot yet be divided into physical variation, aperture placement and instrumental response. A brightness change in raw counts is not a calibrated fluorescence change.

Long RED860 exposures from 29 August were severely saturated and were excluded. The shorter RED860 frames were not reduced. Consequently the named lines at 685.516, 703.824 and 714.815 air nm have no UVES result in this work. The missing entries in Appendix A are not zero filling.

6 Hubble/STIS: a check above Earth's atmosphere

The usable detector regions

Two STIS G430L exposures from Hubble program 12433 were obtained on 27 January 2011. Each lasted 2.5 seconds through the 52 by 0.1 arcsecond slit. The first began at 15:17:26 UTC with CCD gain 1; the second began at 16:53:19 with gain 4. Their pointings differ. They are not a controlled temporal pair. The nominal dispersion is about 0.273 nm per pixel and the quoted resolution for these Venus observations is about 0.54 nm, so groups of solar lines are blended.

The bright portion of the gain-1 image is saturated and was excluded. All nonzero data-quality flags were masked, and saturation masks were expanded by two pixels. Four gain-1 bins, rows 420–499 in groups of twenty, remained in the main green analysis. Twelve gain-4 bins were retained: rows 220–259 and 300–499. The slit bar and faint edge were excluded. At least 60% of the rows in a bin had to be valid at each spectral sample.

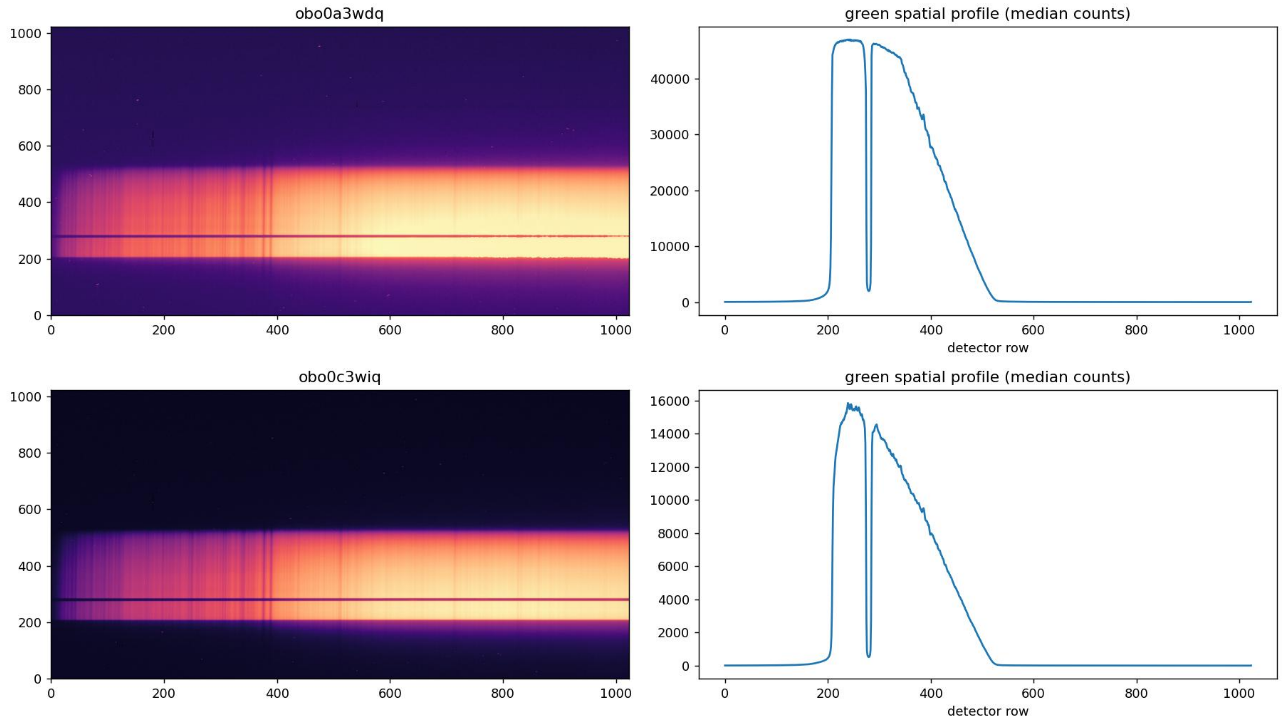

Figure 10. Full STIS detector images and their brightness profiles. The bright saturated gain-1 region is excluded from the fits described in the text. Row numbers are detector coordinates, starting at zero; they have not been converted into a matched map of Venus latitude or UV absorption. The two images sample different pointings.

Each row was normalized locally before averaging, which avoids weighting the brightest rows more strongly merely because of slit illumination. The observed spectral pixels were not resampled. The archive products had wavelength calibration, extraction, rectification and flux calibration marked OMIT, so an initial dispersion was calculated from the official coefficients and a local offset was fitted. The offsets near −0.8 nm absorb wavelength-registration errors; they are not interpreted as Venus winds. A full extended-source CALSTIS reduction was not performed.

The preferred line-spread function was interpolated between the published 320 and 550 nm narrow-slit profiles, with a further Gaussian width fitted. The published profile already includes pixel response and was not convolved with a pixel a second time. An additional slit-illumination convolution was tested separately. The reference uses Baker above 500 nm and Reiners below it.

Green and neighboring spectral intervals

The green blend at 507–537 nm gives q = 10.62% and 10.34% for the two exposures. The neighboring Hβ interval is more sensitive to continuum choice, and the violet intervals are unstable to polynomial degree and edge selection. They are retained as diagnostics but are not used to reconstruct a low-violet emission edge.

Table 4. STIS preferred fits. The spread is the full spatial-bin range. SE is the median conditional error of a bin fit, in percentage points; it is not the uncertainty on the listed median and excludes systematic calibration errors.

Gain	Vacuum interval, nm	Bins	Median q, %	Spatial range, %	SE, points
1	476–498	4	5.65	5.26–6.17	1.56
4	476–498	11	4.83	4.29–5.79	1.55

Gain	Vacuum interval, nm	Bins	Median q, %	Spatial range, %	SE, points
1	507–537	4	10.62	9.96–11.51	0.87
4	507–537	12	10.34	8.05–11.15	0.85
1	538–560	4	9.33	6.25–12.50	2.10
4	538–560	12	9.38	5.55–11.94	1.72

The green f values, summarized over the same bins, are about 11.88% and 11.53%. The higher STIS coefficients cannot yet be assigned to a physical change from the 2018 ground-based observations. Different resolution, locations, geometries and instrumental responses are involved.

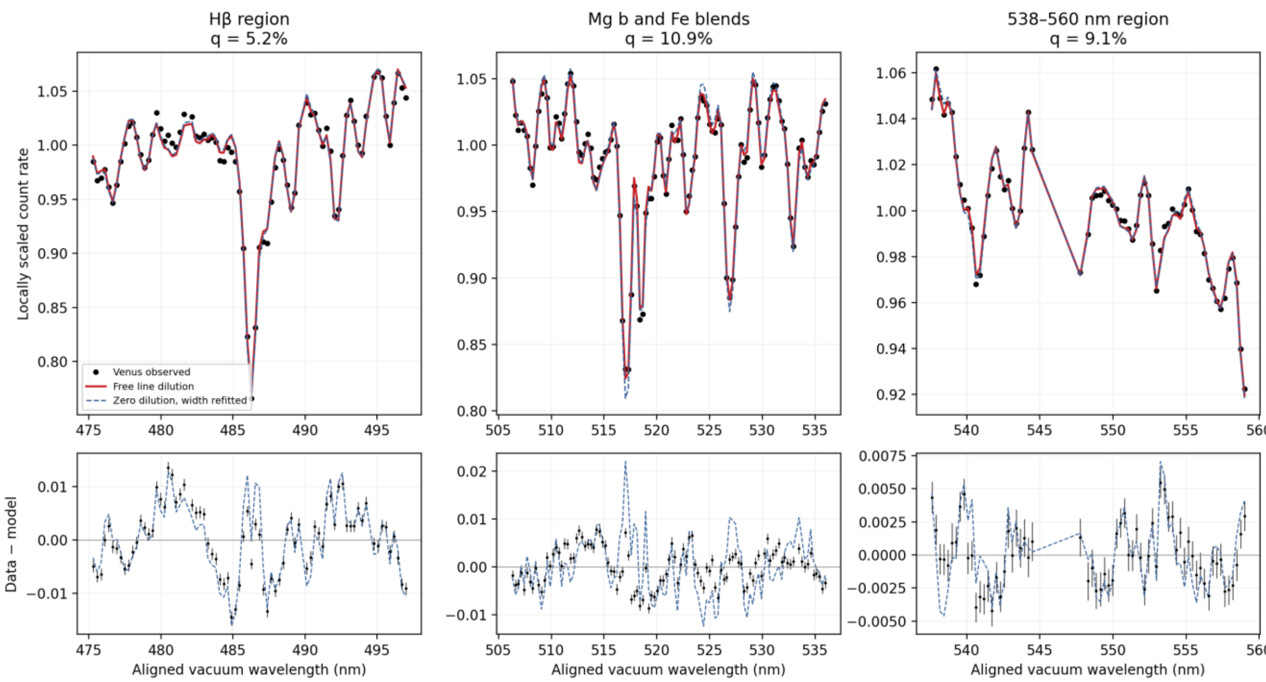

Figure 11. Actual STIS solar-line blends with the preferred positive-q model and a separately fitted q = 0 model. Width, wavelength shift and continuum are reoptimized for the zero-addition comparison. In the representative green bin, the normalized RMS falls from about 0.61% to 0.38% when q is fitted. This is an improvement within the tested model family, not a fluorescence identification.

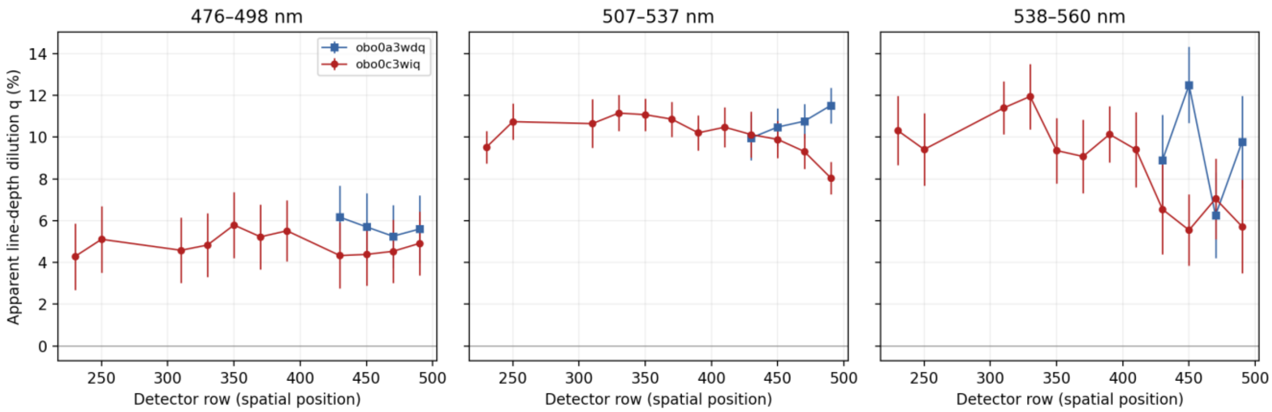

Figure 12. STIS coefficients across accepted detector-row bins. Error bars are conditional local fit errors scaled by the residual variance. Positive green filling remains in both exposures. The points do not establish a geographical fluorescence map, since no corresponding registered UV map or complete extended-source response is available.

Background, reference and profile checks

The measured off-planet background was about 0.11% of the source in gain 1 and 0.05% in gain 4. Its subtraction changed green q by at most about 0.1 percentage points. This excludes that measured background as the main addition. It does not measure light redistributed inside the bright planetary spectrum by the optics.

Using the telluric-clean Baker reference lowered a representative green result from 12.1% to 10.9%, and the 538–560 nm result from 15.3% to 9.1%. The latter older value is superseded. Quadratic, cubic and quartic continua gave green q of 10.9%, 10.5% and 11.3%; a linear continuum gave 15.3% with poorer residuals. Hβ changed much more, from about 0.5% to 9.1% across those choices.

Fine, flux-conserving sampling of the solar reference changed green and Hβ q by less than 0.02 points. Allowing a local wavelength stretch changed green q by less than 0.01 points. In thirty-realization injection tests, input q of 0%, 5% and 12% was recovered as −0.04%, 4.99% and 11.97%. Stricter saturation masks and ten-row bins also retained the green addition.

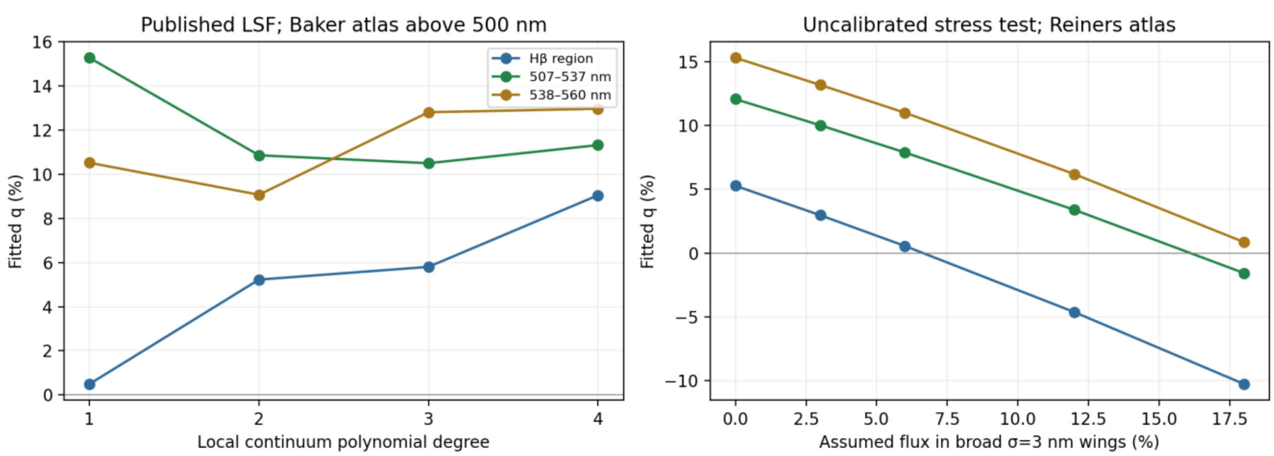

Figure 13. Left: STIS sensitivity to continuum degree with the published instrumental profile and Baker reference above 500 nm. Right: an uncalibrated broad-wing stress test using the Reiners reference. The latter shows that sufficiently broad redistribution can replace much of an apparent addition; those wings were not measured in STIS. The extraction and violet diagnostics discussed in the text are separate tests.

A hypothetical halo containing 12% of the response with a dispersion of 3 nm can manufacture apparent q near 8.9%. That halo is far broader than the published narrow-slit profile, whose tabulated area outside two pixels is only about 0.045% at 550 nm. It is a deliberately uncalibrated stress test, not an observed property of STIS. The real response to extended Venus illumination still needs direct verification.

The direct Venus-to-Hubble light path does not cross Earth's lower atmosphere. Terrestrial atmospheric Raman scattering and absorption on that path therefore cannot explain the STIS result. A terrestrial imprint in the reference atlas, telescope stray light and Venus's own Raman scattering remain separate questions. The positive STIS result is useful because it changes which explanations can apply across all instruments.

7 A conditional reconstruction of the added-light spectrum

The fitted wavelength dependence of f is not itself an emission spectrum. If the addition is fluorescence, f represents its intensity divided by a reflected continuum that changes with wavelength. To estimate the shape of the addition, the reflected spectrum must also be estimated.

The main reconstruction uses the direct ESPRESSO/Vesta fits. This choice keeps the wavelength sampling, observing mode and reference treatment consistent. The other instruments are kept as independent comparisons. They have not been averaged into the same curve, because their calibration and sampled clouds differ.

Let $\bar{T}$ be the assumed mean total spectrum in a fitting window, and $\bar{S}$ the mean of the normalized Vesta template. With a locally constant continuum, the window mean is $\bar{T} = C(\bar{S} + f)$. Therefore

$$F_{proxy}(\lambda) = f(\lambda)\,\bar{T}(\lambda) / [\bar{S}(\lambda) + f(\lambda)]. \quad (4)$$

For $\bar{T}$, the digitized 2020 reflectivity curve in Lee et al. (2022) was multiplied by the TSIS-1 Hybrid Solar Reference Spectrum at one-nanometer sampling (Coddington et al. 2023). The adopted reflectivity includes blue spectroscopy and visible photometric anchors near an 80° phase angle. It was not measured with the 2018 ESPRESSO exposures. This makes the reconstruction conditional on a noncontemporaneous continuum calibration and on its phase dependence. The unknown common geometric scale disappears on normalization, but a wavelength-dependent calibration error does not.

The 1,716 accepted direct-reference fits were converted from vacuum to air wavelength. The end centers at 408 and 713 vacuum nm were omitted because the archived continuum reference did not cover their converted positions. The remaining 1,650 values cover 50 window centers in 33 exposures. A median was calculated at each center. For display, a three-window median was followed by local linear smoothing with a Gaussian bandwidth of 10 nm. Endpoints were preserved and gaps wider than 6 nm were left open. Both the median points and the displayed curve were divided by the maximum of the displayed curve.

The result is a broad blue-green addition that decreases toward the red. The displayed maximum is near 478 nm. That number depends on the continuum model and smoothing; it is not a measured molecular transition wavelength. The violet end remains above half the displayed maximum, so the blue half-maximum point lies outside the reconstructed domain or is not determined. A full width at half maximum cannot be measured from this preferred curve.

The absorption curve is taken from the supplied workbook, cells A4:B94, containing 91 samples between 365 and 455 nm. Its maximum is 1,277.67 at 375 nm in the decadic absorption-coefficient convention of the published model. Each curve is normalized separately. Their relative heights in Figure 14 contain no information about fluorescence efficiency. Moreover, the absorption model and the adopted visible continuum partly share the Lee observational foundation; they are not wholly independent data products.

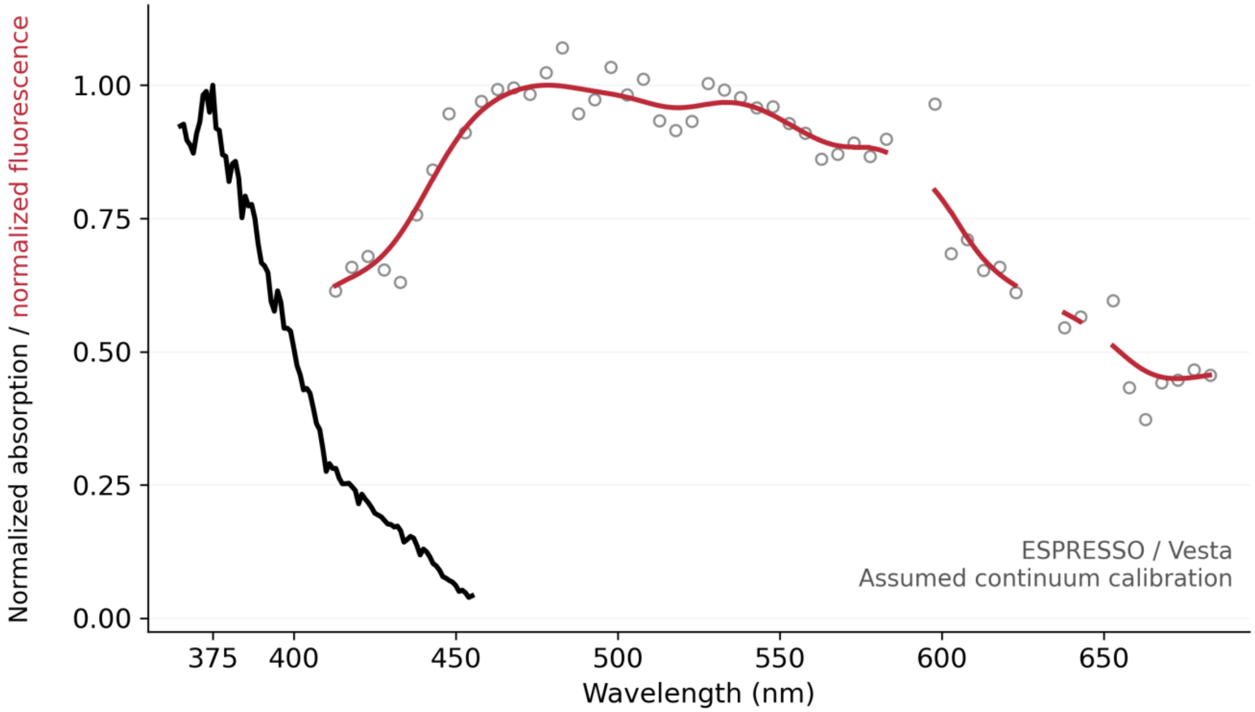

Figure 14. Normalized absorption is shown in black and the conditional added-light spectrum in red, with individual window summaries in gray. The absorption samples were read directly from the supplied 2026 model workbook and divided by their maximum. The added-light samples were calculated from 33 ESPRESSO exposures fitted against Vesta, using equation (4) and an assumed continuum obtained from Lee et al. (2022) reflectivity multiplied by TSIS-1 solar irradiance. Fifty retained window centers were summarized and smoothed as described in the text; gaps remain open. This is a reconstruction from observed line dilution under a continuum assumption, not a direct calibrated emission spectrum. No absolute yield or pigment identification is implied by the overlay.

The earlier CFHT reconstruction is retained in Appendix B. Its sixteen curves represent sixteen exposures, not sixteen solar lines. Those curves used 873 accepted windows and the same general continuum assumption. They were useful for exploring whether the addition could be broad, but the empirical-reference corrections and fibre-contamination checks now take precedence when interpreting the shape.

8 Can other processes produce the line filling?

Fluorescence is one way to add photons inside a solar line. Raman scattering can shift neighboring photons into it. An instrument can redistribute photons from outside the fitted neighborhood. A mismatched reference, an incorrect continuum, or clipping can also make a fitted line appear too shallow. These possibilities must be separated from the chemical question of what could fluoresce.

The tests below cover the known classes relevant to the available observations. Their limits are stated because a failure of one simple model is not a failure of every physical version of that mechanism. No independently calibrated alternative has yet reproduced the complete observed pattern. Full Venus Raman transport and very broad instrumental redistribution have not been excluded.

Rotational and vibrational Raman scattering

In Raman scattering, energy is exchanged between a photon and a molecule's rotational or vibrational state. The outgoing photon changes wavelength. This can fill a solar absorption line and can produce shifted copies of solar features, often called Raman ghosts. Planetary Raman spectra depend on the molecules, temperature, clouds, absorption, illumination and viewing geometry (Brinkmann 1968; Cochran et al. 1981; Oklopčić et al. 2016).

CO_2 is the main relevant gas on Venus. A single-event rotational model was calculated with rotational constant B = 0.39020 cm^{-1}, the allowed even-J populations, and Stokes and anti-Stokes branches with $\Delta J = \pm 2$. Temperatures of 230 and 300 K were tested. A nitrogen template at 250 K was also used as a diagnostic. The shifted solar spectra were fitted with free amplitudes. This tests their local spectral shapes. It is not a multiple-scattering calculation through Venus's clouds.

The 230 K CO_2-only model left green residual sums about 9%, 44%, 28%, 10% and 10% larger than the smooth-addition model in the five representative Venus spectra. The 300 K template improved some comparisons but did not remove the need for a smoother component in these cases. When a smooth term and a Raman template were both allowed, the green smooth term remained positive.

Table 5. Representative CFHT green offsets before and after adding the tested CO_2 rotational template. The last column is the remaining smooth addition divided by reflected continuum. All entries are percentages; these are model comparisons, not separately detected emission components.

CFHT product	Observation	Original f	Equivalent q	Remaining smooth f
1688583i	February 2014	4.28	4.10	3.81
1701532i	April 2014	12.81	11.36	10.10
1887392i	January 2016	13.00	11.50	10.19
2298946i	August 2018	9.67	8.82	7.93
2298984i	August 2018	9.16	8.39	7.09

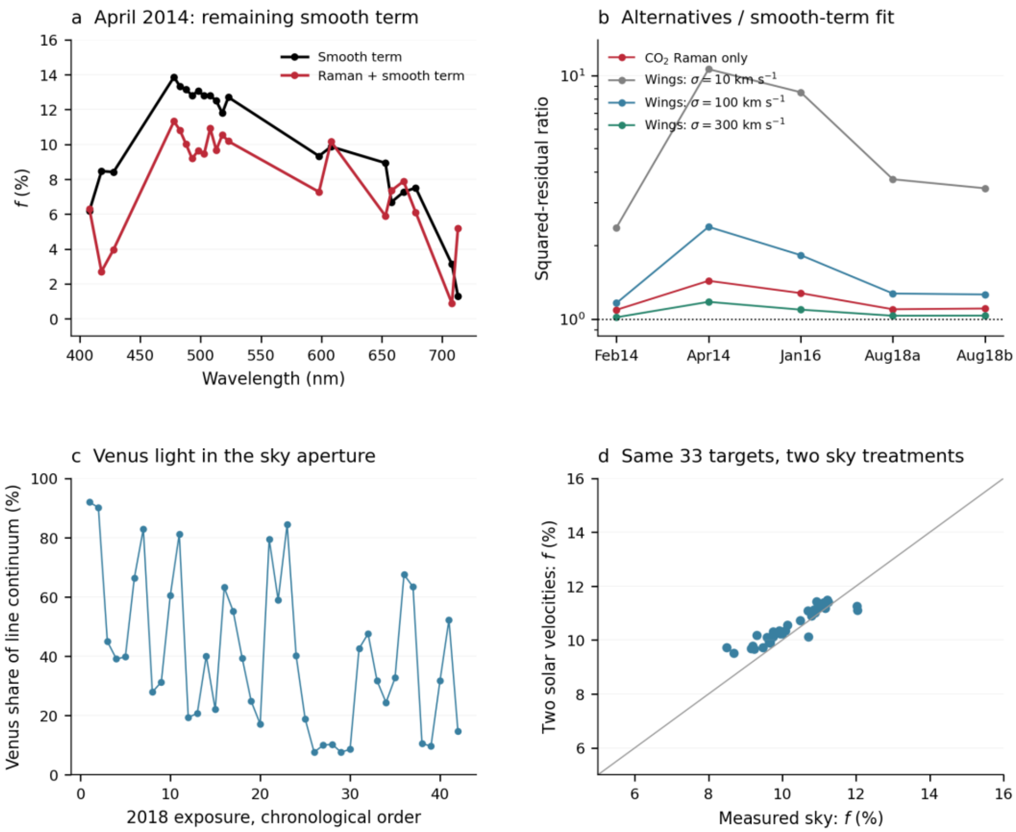

Figure 15. CFHT alternative-model and sky checks. Panels (a) and (b) compare smooth additions, single-event rotational Raman templates and broadened instrumental profiles through their remaining offsets and residual sums. Panels (c) and (d) show Venus contamination in the nominal sky fibre and the paired comparison of sky treatments for the same 33 targets. The tested Raman shapes do not fully replace the larger offsets, while sufficiently broad instrumental redistribution can approach an additive fit. A full Venus Raman atmosphere and the broad instrumental response have not been independently calibrated.

A scale estimate was also made. A 40 mbar gas column, with mean molecular mass appropriate to 96.5% CO_2 and 3.5% N_2 and Venus gravity 8.87 m s^{-2}, contains about 6.25×10^{27} molecules m^{-2}. With the adopted CO_2 differential rotational Raman cross section at 500 nm, 1.58×10^{-32} m^2 sr^{-1}, scaled from the 488 nm backscatter measurement by $(488/500)^4$, multiplication by 4π gives an illustrative optical-depth scale near 0.0012. The angular factor is approximate. This is a single-path scale, not a prediction of observed line filling; repeated scattering and path selection in clouds have not been included (Penney et al. 1974).

Brinkmann's often-cited CO_2 estimate near 15% comes from an idealized aerosol-free calculation whose assumptions were explicitly unsuitable for a full interpretation of Earth-based Venus observations. It should not be used either to explain the present coefficients numerically or to dismiss them. A proper comparison requires the actual cloud and gas transport.

Nor does a λ^{-4} scattering dependence require the retrieved coefficient to decrease smoothly from violet to red. The coefficient is a ratio to reflected light. Wavelength-dependent absorption changes the photon paths and the denominator. Multiple scattering, rotational and vibrational redistribution, and the solar line pattern can further change its apparent shape.

Recent Earth calculations make the same methodological point. Raman scattering can create apparent SIF over barren regions and can leave spatial and seasonal structure after empirical correction. Sanghavi et al. (2025) found modeled false SIF up to about 0.35 mW m^{-2} sr^{-1} nm^{-1} and residual correction errors around ±0.15 in their Earth cases. Those numbers are not Venus predictions. They show why temporal variation and a smooth retrieved component cannot, by themselves, eliminate Raman scattering.

Liquid Raman scattering was considered only at an illustrative scale. A published pure-water coefficient for the 3400 cm^{-1} Raman band excited at 488 nm gives a single-pass probability around 2.7×10^{-7} across one millimeter. This pure-water benchmark (Bartlett et al. 1998) is not a bound for concentrated sulfuric acid droplets, their multiple scattering, or any dissolved material. No laboratory acid-droplet Raman spectrum was fitted to the Venus data. That measurement belongs in the next round of tests.

Instrumental redistribution and line broadening

A narrow Gaussian core was fitted in the high-resolution measurements, while several core and wing models were tested for STIS. This removes ordinary width mismatch within those families. It does not describe arbitrarily broad scattered light. A sufficiently broad positive redistribution kernel draws continuum photons into many line cores and can resemble a smooth addition within a short window.

For CFHT, 10 km s^{-1} wings fitted substantially worse than a smooth addition. At 100 km s^{-1} the residual-sum ratios were still about 1.16–2.39. At 300 km s^{-1} they approached 1.02–1.18, with wing areas of roughly 4.6% for the low-offset case and 9.4–12.3% for the high-offset cases. A 300 km s^{-1} Gaussian has a wavelength dispersion of about 0.50 nm and a full width near 1.18 nm at 500 nm. This is very broad compared with the resolved core.

ESPRESSO and STIS stress tests reached a similar mathematical ambiguity with their respective very broad halos. Such halos have not been established as actual properties of the instruments. The agreement among different instruments makes a single hardware defect less persuasive, but does not remove shared reference errors or a common mismatch between compact calibration sources and extended Venus illumination.

The required test is direct measurement of the instrumental response far beyond the core, under the relevant illumination. A coeval airless reflector helps, as does a bright extended calibration source. Core matching alone is insufficient if the proposed alternative resides in distant wings.

Velocity distributions also matter. Venus winds, the finite solar disk, rotation, aperture motion and slit illumination can combine slightly shifted spectra. Solar center-to-limb line changes and the geometry known as the Young effect can alter planetary Doppler profiles (Gaulme et al. 2018). The fitted shift and Gaussian width absorb part of this behavior; they do not constitute a full disk-weighting calculation. Jupiter's greater rotational broadening is a further reason to use its result as a qualitative Raman comparison, without subtracting it as a Venus baseline.

Earth's atmosphere, sky fibres and solar references

The CFHT 2018 second fibre was separated by about eight arcseconds while Venus was about twenty-six arcseconds across. Its spectrum contains a Venus-velocity component. The median ratio of Venus to terrestrial line-bearing coefficients was about 0.64, corresponding to about 39% of their combined line-bearing continuum. It was not a pure sky measurement. Replacing that measured spectrum with two solar templates gave a median paired change in green f of about +0.27 percentage points across the 33 accepted target spectra, leaving a median near 10.30%. The positive offset survived, while the original sky and spatial interpretation required revision.

ESPRESSO's larger apparent subtraction-induced variability is described in Section 4. These cases show that a sky label in an archive is not enough: the spectrum's velocity must be checked. Terrestrial oxygen, water absorption and atlas residuals were masked or tested with alternative references. Their importance grows around broad Balmer profiles and red atmospheric bands. Hubble removes Earth's lower atmosphere from the direct observing path, while retaining reference and telescope questions.

Temporal differences cannot automatically eliminate an instrument or atmospheric explanation. Illumination, sky contamination, focus, pointing, extinction and detector state also change with time.

The relevant question is whether a calibrated physical emission changes after those effects are accounted for.

Detector, extraction and continuum errors

The raw-level checks, masks, alternative continuum orders, normalized and unnormalized CFHT products, UVES bias test, unmerged BLUE test and STIS saturation exclusions all address parts of this class. They make simple widespread clipping, a single bias-trap artifact, or one particular continuum order poor explanations of the full retained green signal.

There is still no complete independent detector-linearity and scattered-light calibration for every observation. The sparse saturated Ceres pixels in the original CFHT control, the UVES BLUE error propagation, and the omitted STIS calibration stages are retained in the record. Formal small fit errors do not erase those limitations. Polarization-dependent throughput and Stokes cross-talk were not explicitly modeled in the intensity retrievals.

Thermal emission, airglow and other additions

Ordinary elastic Rayleigh or Mie scattering redirects photons without changing their wavelengths. It therefore preserves a local solar line pattern unless other effects, including velocity mixing, are introduced. Broad absorbers can change the continuum color, photon paths and sampling depth, but smooth absorption alone does not add photons to Fraunhofer cores. Molecular absorption can complicate local fits and should be included where relevant.

Thermal radiation is much too faint in the green. Even a 735 K blackbody viewed without cloud attenuation has a 500 nm spectral radiance of only about 3.79×10^{-11} W m^{-2} sr^{-1} nm^{-1}. Against an illustrative reflected continuum of 0.1 W m^{-2} sr^{-1} nm^{-1}, the ratio is 3.8×10^{-10}. The illustrative continuum is not a measurement of these exposures. The temperature calculation shows the scale of the mismatch, and actual cloud obscuration only reduces the surface contribution.

Known Venus airglow and auroral emissions occur in particular atomic or molecular features (Slanger et al. 2001; Gray et al. 2025). They should be tested at their own wavelengths, but isolated lines do not explain a smooth addition recovered in many unrelated solar-line neighborhoods. For scale, one Rayleigh at 500 nm is 3.16×10^{-10} W m^{-2} sr^{-1} integrated over the emission. Even 10 kR spread uniformly across 100 nm would contribute about 3.2×10^{-7} of the illustrative continuum above. This is a dimensional example, not a universal upper bound on unknown dayside emission.

Thomson scattering by an illustrative electron column of 10^{20} m^{-2} has optical depth only 6.65×10^{-9}. Thermal molecular Doppler redistribution is also narrow: the characteristic CO_2 backscatter velocity scale at 250 K is about 0.43 km s^{-1}, much smaller than the very broad halos needed in the stress tests. Lightning, meteors and an unspecified chemical glow were not observed in coincidence with these spectra and have not been shown to reproduce the broad, repeatable pattern. Their mere names do not supply a fitted explanation, but an unknown emitter cannot be excluded by assuming its brightness or spectrum.

Finally, fluorescence need not be biological. Abiotic organic molecules, mineral species or other dissolved emitters would be chemical alternatives if fluorescence were established. Raman and instrumental redistribution are alternatives to fluorescence itself. These are different questions and require different tests.

Table 6. Status of the principal alternatives. “Tested” refers to the stated implementation, not every possible model in the same class.

Explanation	Test and result	What remains

Explanation	Test and result	What remains
CO_2 rotational Raman	Single-event templates leave positive smooth residuals in five CFHT cases	Full cloud transport, multiple and vibrational Raman scattering
Narrow instrumental width	Width fitting and several profile families retain positive green q	Measured very broad wings under extended illumination
Terrestrial sky	Velocity separation and second-template fits; Hubble check	Exact fibre footprints, changing sky and telescope stray light
Solar-reference mismatch	Airless controls and telluric-clean reference preserve green filling	Coeval same-instrument extended-source calibration; violet zero level
Saturation and extraction	Raw-level checks, masks, bias and unmerged-order controls	Full nonlinearity and propagation calibration for all frames
Continuum and sampling	Window/degree changes, fine solar sampling and injections	Some broad Balmer and violet intervals remain unstable
Velocity and polarization effects	Local velocity and width fitted	Full disk-weighted and polarized instrumental forward models
Thermal and electron scattering	Illustrative physical scales far below percent-level green addition	No plausible magnitude shown for these mechanisms
Known narrow airglow	Spectral form and illustrative energy scale examined	Dedicated coincident dayglow constraints; unspecified emitters
Abiotic fluorescence	Compatible with a smooth addition in principle	Laboratory spectra, yields and chemical identification

9 Comparison with fluorescence on Earth

The Earth comparison motivated the measurement method. It also provides a useful brightness scale, provided that the denominators and observing locations are kept explicit. A fraction of light measured inside seawater is not directly comparable with a fraction measured above an atmosphere. None of these fractions is a fluorescence quantum yield.

Land-plant chlorophyll fluorescence is commonly about 1–5% of the much larger reflected signal at the red and far-red wavelengths used for retrieval (Joiner et al. 2012). In the simple notation of this report, this is approximately f = 1–5%, or q = 0.99–4.76%. It is an indicative range, not a universal upper limit for leaves, canopies or all observing geometries.

Hu and Voss (1998) measured solar-stimulated marine fluorescence near 689 nm as about 15% of in-water upwelling light near the surface and 42% at four meters depth in their observations. The corresponding ratios to all nonfluorescent light would be 17.6% and 72.4%. That background includes processes such as Raman scattering, so these converted values are not necessarily ratios to purely elastic reflection. The high fraction at depth partly reflects attenuation of the background; it does not imply an extraordinary quantum yield.

At the top of the atmosphere, Köhler et al. (2020) reported an ocean example in which red fluorescence contributed up to about 10% of the measured signal. That selected dark-ocean scene is a useful remote-sensing comparison with the Venus coefficients. It is not a global ocean mean. Wolanin et al. (2015) had earlier retrieved marine fluorescence through the Fe I feature near 684.3 nm. Their example differential optical-depth signal of a few thousandths is not q or f and has not been converted into a Venus-comparable percentage here.

Table 7. Brightness comparisons. Venus entries remain apparent added light under the fitted model. Earth entries are reported fluorescence quantities from the cited studies. No Earth raw spectra were reanalyzed for this report.

Observation	Reported or fitted fraction	Observing level and meaning
Venus, ESPRESSO/Vesta	q = 6.24%; f = 6.66%	Green continuum; sampled Venus aperture
Venus, UVES RED	q ≈ 6.0–7.2%	Exposure medians in selected green windows
Venus, UVES BLUE	q ≈ 8.5–9.4%	480/490 nm windows; separate arm and calibration
Venus, STIS	q ≈ 10.3–10.6%	507–537 nm blends, accepted spatial bins
Land chlorophyll	f ≈ 1–5%; q ≈ 1.0–4.8%	Approximate red/far-red fluorescence relative to reflection
Selected TROPOMI ocean scene	Up to about 10% of total signal	Red fluorescence above Earth's atmosphere
Marine water near surface	About 15% of upwelling light	In-water measurement near 689 nm
Marine water at 4 m	About 42% of upwelling light	In-water measurement near 689 nm

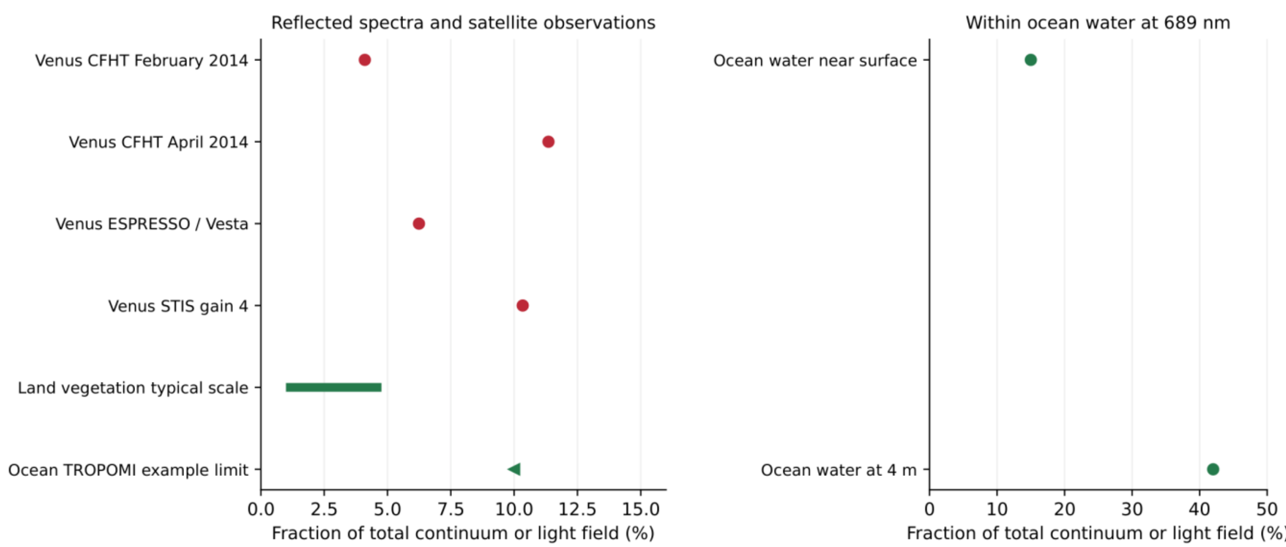

Figure 16. Apparent Venus additions and published Earth fluorescence fractions. The in-water marine measurements are placed in a separate panel because their observing level and background differ from remote measurements. The land range is converted from f to q with equation (2). These are descriptive magnitude comparisons, not matched geometries, identical spectral bands, biological efficiencies or proof that the Venus addition is fluorescence.

The retained Venus coefficients are therefore of a measurable scale already encountered in fluorescence observations on Earth. Some exceed the approximate land-plant range; they are not outside every marine fraction. This comparison supports the practicality of the method. It does not establish the source chemistry or close an energy budget for Venus.

The spectral distinction is substantial. Chlorophyll a fluorescence used in remote sensing is red, near 685 nm, with a far-red feature around 730–740 nm in vegetation. The conditional Venus reconstruction is blue-green. Blue-green fluorescence is known from other organic compounds, including plant phenolics, but this does not identify a Venus molecule (Lichtenthaler and Schweiger 1998).

The earlier suggestion that the reconstructed width matches chlorophyll b is not supported. The historical CFHT curves have conditional widths of roughly 215–241 nm under their assumed continuum. They are much broader than the principal molecular chlorophyll-b fluorescence band. The preferred ESPRESSO reconstruction lacks a measured blue half-maximum and therefore has no securely determined full width. Laboratory pigment spectra also depend on solvent, binding and excitation. Neither a broad curve nor a convenient normalization supplies a chlorophyll match (Dixon et al. 2005; Taniguchi and Lindsey 2021).

10 Should fluorescence follow the UV-dark clouds?

What the available correlation tests show

The proposed correlation was reasonable as a test: if the same material absorbs the excitation light and emits fluorescence, more of it may increase both UV darkness and emitted light. It was too strong to expect a one-to-one relation in every image. The absorption and emission can sample different depths, and the measured coefficient divides the emission by a changing reflected continuum.

The CFHT color proxy was calculated from extracted counts as

$$A_{color} = -\ln[C(378\text{–}388\ \text{nm}) / C(598\text{–}608\ \text{nm})]. \quad (5)$$

This is an instrumental UV-to-red color, not a calibrated absorber column. Airmass, throughput, extinction, seeing, sky subtraction and aperture placement can all affect it. Partial rank correlations were calculated while controlling for airmass, fitted green sky contribution and the logarithm of the red count rate. Serial observations were not assumed to be independent samples of a global relation.

The correlations change sign between scans. The April 2014 sequence gives a positive partial correlation of about +0.56 between green f and the color proxy. February scans and August 2018 do not repeat that sign consistently. The correlation with green-minus-violet filling is weaker. In the revised 2018 two-solar-template treatment, the same 33 accepted spectra give about −0.59 for green filling and −0.27 for green-minus-violet filling.

Table 8. CFHT partial Spearman correlations. The two response columns are green f and the difference between green and violet f. The controls are airmass, fitted green sky contribution and log red count rate. These are scan-level associations, not detections of absorber–fluorescence coupling.

Date	Accepted spectra	Green f	Green minus violet f
8 Feb 2014	16	+0.18	+0.11
9 Feb 2014	18	−0.27	−0.40
10 Feb 2014	17	−0.41	−0.30

Date	Accepted spectra	Green f	Green minus violet f
16 Apr 2014	36	+0.56	+0.31
22 Aug 2018, original treatment	33	−0.45	−0.09
22 Aug 2018, two solar templates	33	−0.59	−0.27

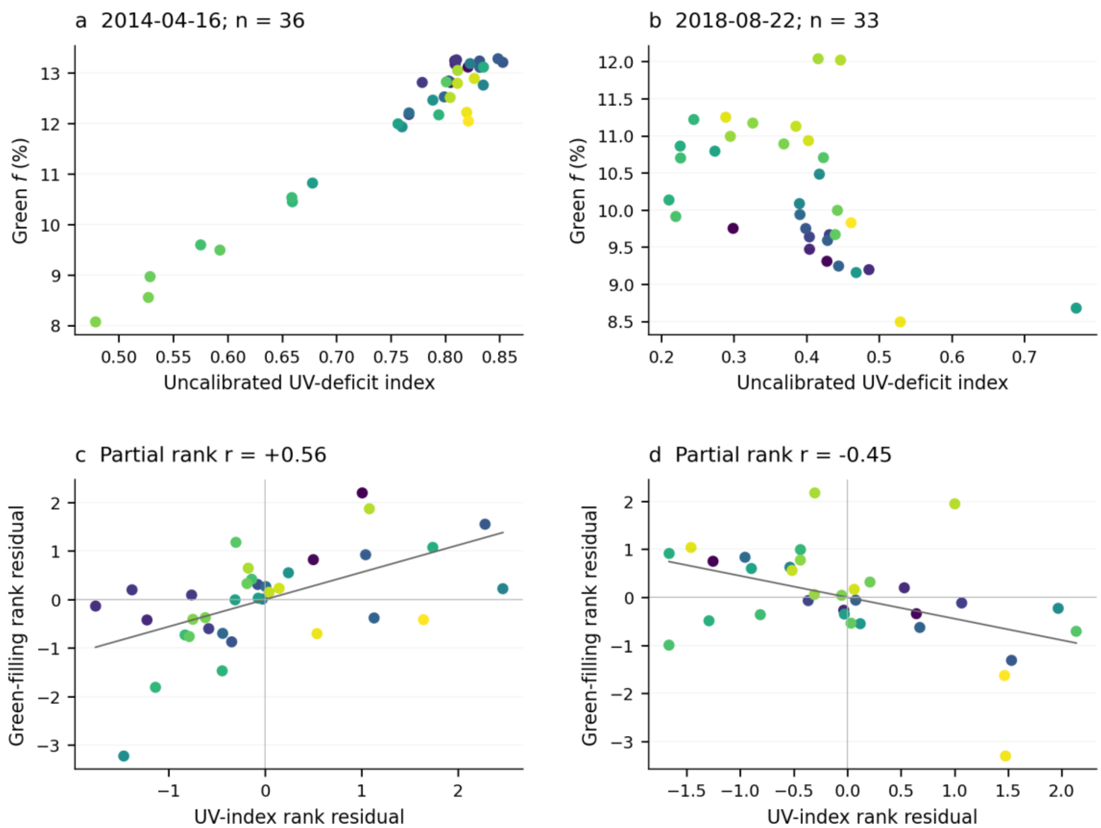

Figure 17. Original CFHT color and line-filling comparisons with scan diagnostics. The April association is positive, while other scans give weak or negative associations. Colors show elapsed time within each scan, from purple for earlier observations to yellow for later ones. The revised 2018 sky treatment in Table 8 should be used for the updated numerical interpretation. A single raw color correlation does not identify the emitting layer or remove observing-condition effects.

Between February and April 2014, green f changed from roughly 4.1–4.4% to 12.6%, while green-minus-violet filling changed only from about 3.4–3.5 to 4.3 percentage points. Much of the change therefore resembles a broad baseline shift. February twilight and April daylight observations had different sky conditions. The detector history and documented 2018 instrument difficulties were also recorded as possible confounders, not assumed explanations.

The nearest recovered 2016 photometry was about 38–41 days from the relevant spectra and cannot provide a simultaneous absorber comparison. The available 2018 Akatsuki maps were about 3.20 hours before and 6.80 hours after the CFHT observations. After the geometric cuts, no usable overlapping region with reliable aperture registration remained. Thus a spatial correlation with mapped UV absorption was not obtained. The STIS and UVES row plots do not repair this missing registration.

Absorption and emission weight different depths

UV imaging measures reflected light after it has traveled through the cloud. A model can assign much of the contrast near 365 nm to the upper several kilometers, but that weighting depends on wavelength and cloud assumptions (Lee et al. 2021). It is not a hard lower boundary on all material that can contribute fluorescence.

For emission at wavelength λe, a schematic photon contribution from depth z can be written

$$N_F(\lambda e) \propto \int dz\, n(z)\, P_{escape}(\lambda e,z) \int d\lambda x\, \sigma_{abs}(\lambda x,z)\, J_{ph}(\lambda x,z)\, \Phi(\lambda e \mid \lambda x,z). \quad (6)$$

Here n is emitter abundance, J_ph the local excitation photon field, σ_abs its absorption cross section, P_escape the probability that an emitted photon reaches the observer, and Φ the emitted spectrum per absorbed photon. This equation is a statement of the depth weighting, not a fitted Venus model. Excitation and escape can sample different depths from the observed UV contrast. Solar energy remains available inside parts of the clouds, but its spectrum and intensity change with depth (Mogul et al. 2021).

For ordinary Stokes fluorescence near 500 nm, excitation photons must generally be shorter in wavelength than the emitted photons. Red light penetrating more deeply cannot by itself pump green fluorescence without another energy source or a different upconversion mechanism. A deeper-emission explanation must therefore calculate both the relevant blue/UV excitation and the escape of green photons.

If more emitting absorber is added to a thin, equally illuminated layer with fixed yield, UV darkness and fluorescence should initially increase together. Once absorption saturates, adding more material may barely change the UV image. A high absorbing layer can screen excitation from a deeper emitter and cause an anticorrelation. Emission from a separate deeper population may vary largely independently of the upper UV texture. Concentration quenching and reabsorption can further change the relation. Finally, f can rise because the reflected continuum falls even if the absolute emitted radiance does not increase.

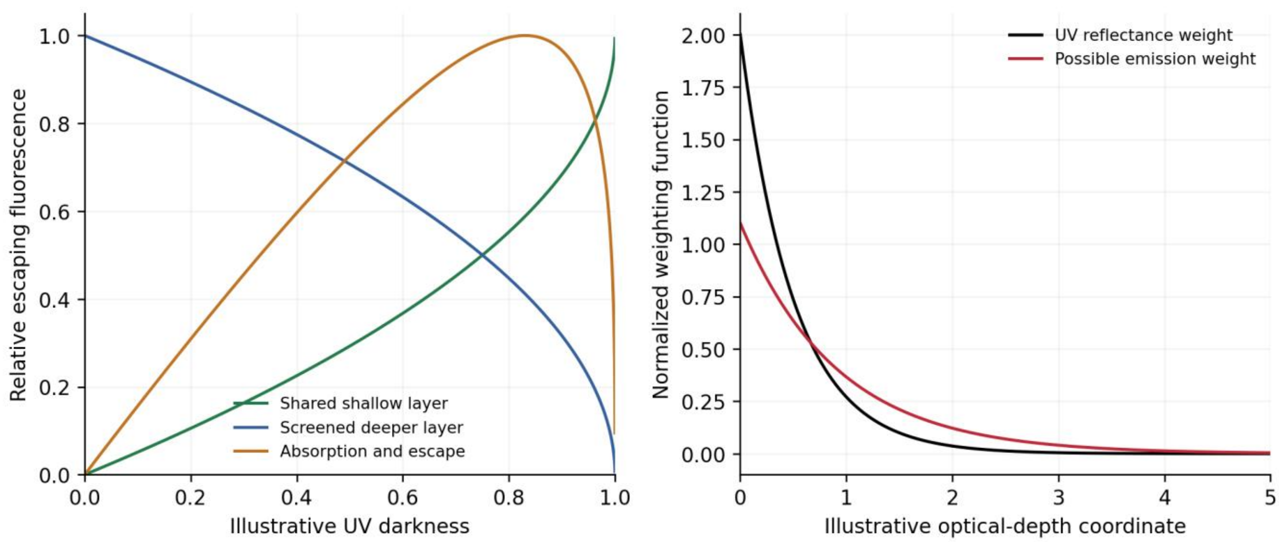

Figure 18. Illustrative depth weighting and screening, calculated from simple exponential functions. The right-hand horizontal coordinate is optical depth, not kilometers; the left-hand coordinate is UV darkness. The curves show how a shallow common absorber/emitter can give a positive relation, how an upper screen can suppress a deeper source, and how competing absorption and escape can produce a turnover. The left-hand curves are scaled for display; the right-hand weighting functions integrate to one over infinite depth. These are demonstrations of possible behavior, not fits to Venus data or estimates of its emitting altitude. The functions and sampled values are included in the calculation files.

The absence of a perfect correlation therefore does not negate fluorescence. It also does not confirm a hidden deeper source. The needed test is a registered, simultaneous measurement of UV reflectance and absolute added radiance, interpreted with a common cloud model.

The claim about UV line filling and cloud topography

The claim that UV line filling directly gives exact cloud-top topography, localized pressure systems and gravity waves combines different observations. Raman filling can depend on gas paths, but no single coefficient gives an exact gas column independent of clouds, absorption and geometry.

Akatsuki IR2 cloud-height retrievals use CO_2 absorption near 2.02 micrometers, not the UV Fraunhofer-filling method. The inferred height is tied to optical depth in an assumed cloud model. It can reveal height structure and wave-related patterns, but it is not an exact geometric surface or a complete pressure map (Sato et al. 2020). Such cloud-height constraints would be valuable inputs to a Venus Raman calculation. They do not already explain the green filling measured here.

11 Tests that would decide more

The aim is an observational case, not a mathematical proof. Fluorescence would become a much better established interpretation if a common emitted spectrum survived independent instrumental calibration and a quantitative Raman calculation, and if its excitation or particle emission were measured directly. Several practical tests follow from the present results.

First, the broad instrumental response should be measured under Venus-like illumination. An observing sequence with Venus, nearby blank sky and an airless solar reflector should use the same setting and track the full line profiles. Sky apertures must be registered on the sky and checked by Doppler shift. The same Venus region should be repeated through different aperture placements. A fit should reproduce weak and strong solar lines with one physically consistent smooth emission spectrum and an independently measured instrumental response.

Second, a Venus radiative-transfer calculation should include CO_2 rotational and vibrational Raman scattering, multiple cloud scattering, wavelength-dependent absorption and the measured viewing geometry. Its predicted shifted solar ghosts and its dilution of different line strengths should be tested together. A free local Raman amplitude is useful for diagnosis but does not replace this calculation. Agreement with the independently constrained Raman component would allow any remaining smooth emission to be assessed quantitatively.

Third, simultaneous UV imaging and visible spectroscopy should be registered to the same cloud regions. The recovered quantity should include absolute added radiance, not only f or q. Repeating the measurements over phase angle and cloud texture would test excitation, escape and depth predictions. A slit scan or suitable integral-field spectrograph could provide this spatial information. The present archive spectra demonstrate that enough light reaches large ground-based telescopes to measure line depths; calibration is the current limit.

TROPOMI demonstrates the red-fluorescence retrieval principle over Earth, but its existing bands are a poor match to much of the proposed Venus green feature. The official calibrated-band documentation gives a visible endpoint near 499 nm and near-infrared coverage beginning near 661 nm. The intervening green region is absent. Its visible resolution, about 0.45–0.65 nm, also blends narrow solar lines (Kleipool et al. 2018). No Venus photon budget or spacecraft repointing assessment was completed here. An Earth-scene SNR specification is not sufficient to claim that pointing the actual satellite at Venus would establish the signal.

Further high-resolution ground-based archives remain useful, but no additional HIRES, HARPS or ARCES line-filling measurement is claimed in this report. The available HIRES material was an archive inventory, not a reduced confirming spectrum. These instruments would be valuable with suitable Venus data, calibration references and observing geometry.

Fourth, candidate materials should be measured in Venus-relevant sulfuric acid, temperature and concentration ranges. Excitation spectra, emission spectra, yields, quenching, photochemical evolution, Raman scattering and reabsorption are all needed. A broad emission can be compatible with a mixture of molecules without identifying that mixture. Laboratory reproduction would supply a chemical test of the porphyrinoid idea.

An in-cloud particle measurement would provide a different and direct test. The published Autofluorescence Nephelometer design uses 440 nm excitation and detects fluorescence over 470–520 nm while characterizing particle scattering (Baumgardner et al. 2022). Detection of emission from individual cloud particles would test an emitter near the relevant spectral region without relying solely on solar-line subtraction. It would not, by itself, identify the molecule or establish life. The instrument's excitation band also means that it tests materials excitable at 440 nm; an emitter requiring only shorter UV excitation could be missed.

Circular polarization and a biological interpretation

Biological pigments in organized chiral structures can produce characteristic circular-polarization spectra associated with absorption bands (Sparks et al. 2009). A spectrally structured, reproducible signal of this kind would be an important companion to fluorescence. Full Stokes measurements, wavelength-dependent calibration and repeated viewing geometries would be needed.

Circular polarization is not unique to life. Multiple scattering in clouds can generate it even from incident unpolarized sunlight, with geometry-dependent spatial patterns (Rossi and Stam 2018). Instrumental conversion of linear into circular polarization must also be measured. Thus fluorescence plus any nonzero circular polarization would not automatically identify a biosphere.

Life remains a hypothesis worth testing if the same cloud material is shown to absorb, fluoresce and carry a biological-type chiral spectral structure. These observations could build a compelling case for another biosphere if the physical and abiotic alternatives fail quantitative tests. The present data do not rank life as the simplest explanation, because competing cloud, instrumental and chemical models have not yet been compared on equal terms. They also do not identify chlorophyll, porphyrinoids or photosynthesis.

A compact independent review should cover three scientific areas: Venus clouds and UV transfer; SIF retrieval and its biases; and planetary Raman transfer. The instrumental scattering and extended-source calibration require a targeted review by someone familiar with the relevant spectrographs. No external review or reviewer endorsement is claimed here.

12 Conclusion

The search was motivated by the strong cloud absorption inferred in our 2026 paper and by the way fluorescence is measured over plants and plankton on Earth. Solar lines in several public Venus datasets are shallower than matched reflected-sunlight models predict. Positive green filling remains after the specified sky, reference, extraction, continuum, width and detector checks.

The results are consistent with a broad sunlight-induced fluorescence component. The empirical ESPRESSO comparison gives about 6.2% green line-depth dilution. UVES and Hubble also retain positive green additions. The Jupiter calculation is consistent with its known hydrogen Raman filling and shows that the method can detect a real planetary line-filling phenomenon.

No tested alternative has been established as a complete explanation with independently measured parameters. This does not mean that every false positive has been excluded. A full Venus Raman model and a direct calibration of broad instrumental redistribution remain necessary. The strong original claims about a nearly empty violet endpoint and large short-term variability are not retained.

The conditional reconstruction, the independent spectra and the surviving green coefficients justify further observations. Calibrated solar-line measurements, simultaneous UV maps, laboratory acid-cloud experiments, circular-polarization spectra and direct particle fluorescence with an instrument such as AFN can test the interpretation. These tests can establish whether the clouds emit the proposed light and, if they do, what produces it.

Appendix A. The named solar-line neighborhoods

The initial requested red interval began at 652.28 nm. Hα is at about 656.28 air nm; 652.28 nm is not its line center. The later searches extended into the blue and green. The table below retains all 22 named neighborhoods discussed in the analysis, including missing results and masked cores.

The more useful green comparisons include the Fe I neighborhoods near 492.05, 495.76, 527.04 and 532.80 nm. Hβ supplies a broad-profile comparison whose result is more sensitive to continuum choice. The Mg triplet and the pair near 527 nm have overlapping fitting windows and are not independent measurements. Fe I near 667.80 nm and Ni I near 676.78 nm provide red comparisons. The Na D, Hα and far-red neighborhoods require special care with terrestrial absorption, broad wings and rejected core pixels.

Table A1. Representative fits for all 22 named neighborhoods.

Each entry is a fitted four-nm neighbourhood associated with the named feature. Nearby Mg and Fe entries share fitted pixels. None is an isolated transition flux. Wavelengths are nominal air values; minor last-digit differences in the saved lists are retained in the CSV. The UVES and ESPRESSO fits are centred at the corresponding converted vacuum wavelengths. Different dates, resolutions, references and continuum/sky treatments prevent interpreting differences between columns as a measured change in emission.

- CFHT/ESPaDOnS: observation **2298946i**, **22 August 2018**; **f (%)** is added light divided by the fitted Venus-reflected continuum, with the measured second-fibre spectrum also fitted. Its footprint has not been established as blank sky. The retained-core fraction is recorded separately; a fitted neighbourhood remains calculable even if its named core is rejected.
- ESPRESSO: constituent **ADP.2021-04-13T12:10:18.476**, observed **3 September 2018, 23:18:11.267 UTC**, fitted against empirical Vesta **ADP.2021-04-14T14:24:19.877**; **q (%)** is added light divided by the total continuum. These are one-exposure named-window fits, **not 33-exposure medians**. A separate CSV contains all-exposure medians at the regular grid windows.
- UVES RED580: **UVES.2018-08-29T23:13:46.961**, spatial row **32**; **UVES.2018-09-03T23:09:47.826**, row **52**. These are single-row **q (%)** fits, not nightly averages. BLUE values for row 19 on both dates are also included in the full CSV, but omitted from this compact table.
- An em dash denotes a missing or excluded coefficient, never zero. ESPRESSO did not run all 22 exact named centres. UVES RED does not cover the first two violet lines or the three lines beyond 683.5 air nm.
- q = f/(1 + f) only when the continuum under comparison contains the reflected and added components alone. The CFHT additional sky treatment means the table must not be read as comparing equal percentage definitions.

Feature	Air nm	CFHT f, %	ESP q, %	UVES Aug q, %	UVES Sep q, %	Core / qualification
Fe I	438.3545	8.31	5.90	—	—	Window fit
Fe I	440.4751	8.70	6.05	—	—	Window fit
H beta	486.1330	9.48	6.33	6.46	6.64	Broad Balmer profile; continuum-sensitive
Fe I	492.0503	10.27	6.37	6.98	7.14	Window fit
Fe I	495.7597	9.50	6.56	6.85	6.98	Window fit
Mg I b	516.7320	8.26	—	6.24	6.31	Overlapping neighbourhoods
Mg I b	517.2680	8.27	—	6.23	6.33	CFHT core 10% retained; Overlapping neighbourhoods
Mg I b	518.3600	8.43	6.03	6.28	6.35	CFHT core 10% retained; Overlapping neighbourhoods
Fe I	526.9538	8.92	6.69	6.62	6.58	CFHT core 22% retained; Overlapping neighbourhoods
Fe I	527.0356	8.89	6.70	6.60	6.58	Overlapping neighbourhoods

Feature	Air nm	CFHT f, %	ESP q, %	UVES Aug q, %	UVES Sep q, %	Core / qualification
Fe I	532.8039	9.32	6.51	6.89	7.08	Window fit
Fe I	542.9700	9.13	—	6.80	6.78	CFHT core 20% retained
Na I D2	588.9950	7.16	—	4.92	5.17	CFHT core 0% retained; Terrestrial absorption; Core masked
Na I D1	589.5920	5.33	—	5.02	5.22	CFHT core 0% retained; Terrestrial absorption; Core masked
Fe I	617.3340	7.26	—	6.43	6.43	Window fit
Ca I	643.9080	7.41	—	5.35	5.19	CFHT core 43% retained
H alpha	656.2810	5.08	3.84	4.18	4.43	CFHT core 14% retained; Broad Balmer profile; continuum-sensitive
Fe I	667.7990	5.61	3.89	5.51	5.46	Window fit
Ni I	676.7770	7.37	4.46	6.45	5.45	Window fit
Fe I	685.5160	8.03	—	—	—	Far red; diagnostic only
Fe I	703.8240	4.08	—	—	—	CFHT core 43% retained; Far red; diagnostic only
Ca I	714.8150	-0.82	—	—	—	CFHT core 0% retained; Far red; diagnostic only

A returned neighborhood coefficient is not evidence that the named core itself was retained. In the CFHT example, only about 10% of the Mg I 517.27/518.36 nm core samples remain, and the Na D cores are fully masked. The negative Ca I 714.815 nm neighborhood coefficient is retained as a diagnostic. It is not physical negative emission. The complete CSV also includes BLUE UVES rows and all source identifiers. A separate ESPRESSO table gives regular-grid medians near these features; those medians must not be confused with the exact named-window fits printed here.

Appendix B. The sixteen earlier CFHT reconstructions

The historical reconstruction used sixteen exposures in five campaigns: one in February 2014, two in April 2014, two in March 2015, eight in January 2016 and three in August 2018. It contains 873 accepted four-nanometer fits after the stated signal-to-noise and boundary cuts. The reconstruction assumed the borrowed reflectivity and solar irradiance described in Section 7. It did not use raw extracted counts as a calibrated emission spectrum.

The reviewed calculation preserves the first and last points during the running-median step. An earlier endpoint treatment that averaged pairs could blur large red excursions and was replaced. The individual unsmoothed windows are retained in Figure A2. Negative coefficients and high red points were not clipped simply to make a fluorescent band.

Table B1. Historical campaign shapes under the adopted continuum calibration. Width and peak values describe the reconstructed added-energy proxy. They are not intrinsic molecular-band measurements and do not supersede the empirical ESPRESSO reference check.

Campaign	Exposures	Display peak, nm	Interval above 90% of maximum, nm	Conditional FWHM, nm
February 2014	1	489	452–563	215.5
April 2014	2	468	448–546	225.8

Campaign	Exposures	Display peak, nm	Interval above 90% of maximum, nm	Conditional FWHM, nm
March 2015	2	464	448–512	217.2
January 2016	8	491	450–558	229.4
August 2018	3	463	448–531	241.4

Illustrative changes in continuum slope gave widths around 205–250 nm. Changing the smoothing bandwidth from 7 to 15 nm altered the widths by less than about 6 nm. Subtracting an assumed f = 0.02 floor narrowed them to about 182–225 nm. The floor and continuum tilts were sensitivity choices, not measured corrections or a statistical uncertainty distribution. The photon spectrum would be proportional to wavelength times the energy spectrum and would have a different normalized shape.

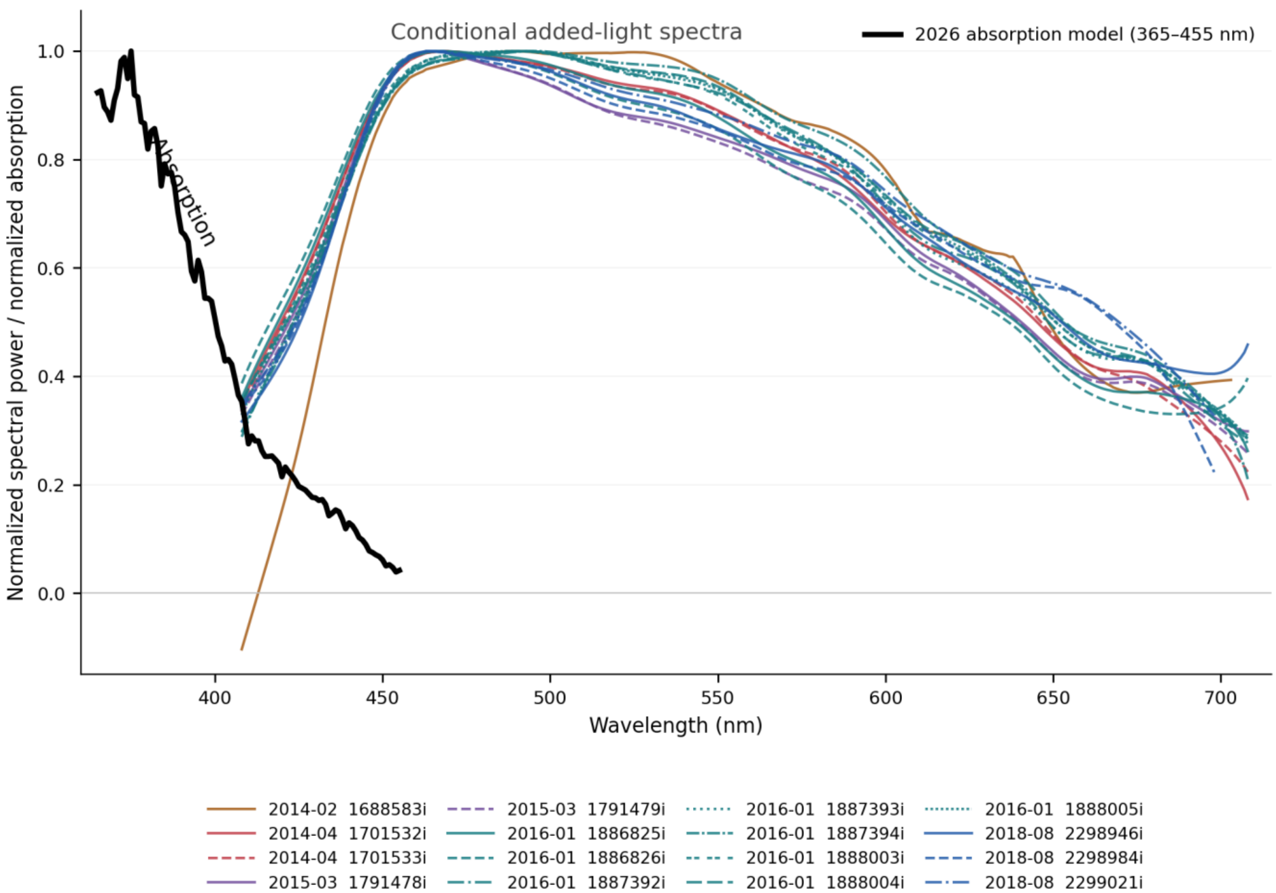

Figure A1. The sixteen reviewed CFHT added-energy reconstructions with their separately normalized absorption comparison. The curves are individual exposures, not sixteen atomic transitions. The assumed continuum, two-solar-component fits and smoothing determine the displayed shapes. The main result in Figure 14 uses the later empirical ESPRESSO/Vesta comparison.

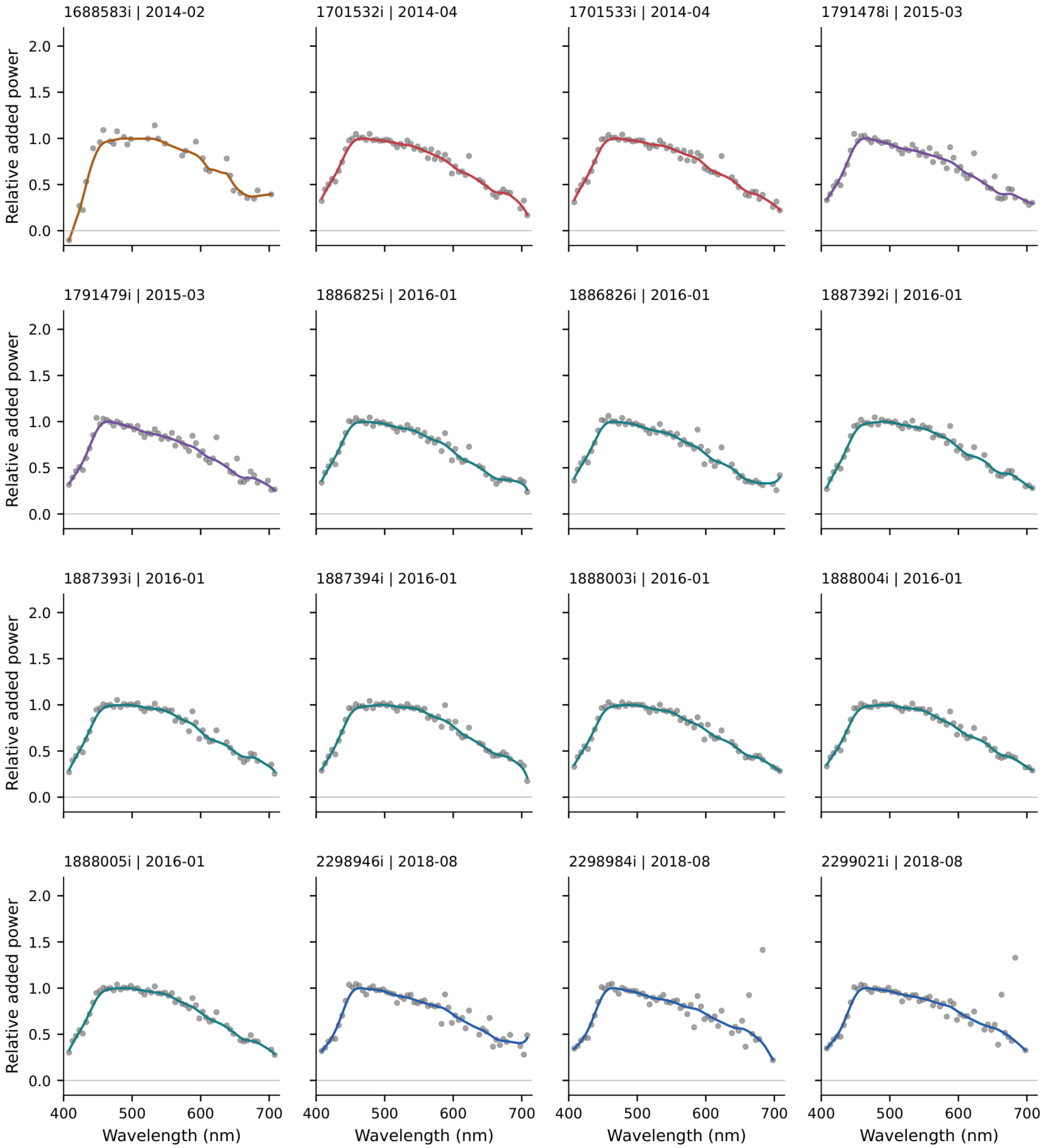

Figure A2. All sixteen CFHT series before display smoothing, together with their reconstructed curves. Each panel retains the accepted individual wavelength-window values, including the red excursions. The accompanying CSV files give the numbers behind every panel and the exposure-level shape metrics. This plot is supplied at full resolution in the calculation attachment for enlargement.

Appendix C. Worked calculations

Conversion between the two reported fractions

For f = 0.10, equation (2) gives q = 0.10/1.10 = 0.090909. For an undiluted depth of 0.70, the observed depth is 0.70 × (1 − 0.090909) = 0.636364. The core rises by 0.063636 of the total continuum. This example explains why the line-core change, q, f and fluorescence yield must not share one percentage label.

For a fitted q = 0.0624228, the corresponding ratio is f = 0.0624228/(1 − 0.0624228) = 0.0665789. This is the rounded ESPRESSO/Vesta green summary conversion. For UVES models containing a separately fitted sky fraction k, the correct Venus-reflected denominator is 1 − q − k.

One reconstructed ESPRESSO window

The saved empirical-reference fit for constituent ADP.2021-04-12T12:27:33.935 at 498.0 vacuum nm, or 497.8611 air nm, gives f = 0.0831234 and q = 0.0767442. Its mean normalized Vesta template is $\bar{S}$ = 0.9095819. The borrowed mean total-spectrum proxy is $\bar{T}$ = 0.4548619 in the arbitrary scale used by the reconstruction.

Equation (4) then gives F_proxy = 0.0831234 × 0.4548619/(0.9095819 + 0.0831234) = 0.0380875 in that same arbitrary scale. This is one exposure/window value, not the median plotted point. Its source row and full precision are saved in worked_reconstruction_example.json. The calculation is repeated by the report asset script and checked against the previously saved reconstruction.

Physical scale estimates

For a blackbody at temperature T, the spectral radiance per nanometer is calculated from

$$B\_\lambda(T) = [2hc^2/\lambda^5] / [\exp(hc/\lambda kT) - 1] \times 10^{-9}. \quad (C1)$$

Here λ is entered in meters. At 735 K, this gives 6.49×10^{-15} at 400 nm, 3.79×10^{-11} at 500 nm, 8.56×10^{-8} at 650 nm and 8.21×10^{-7} W m^{-2} sr^{-1} nm^{-1} at 715 nm. No cloud transmission has been applied, so these are unobscured blackbody values.

For the illustrative 40 mbar atmosphere above a scattering level, the molecular column is N = p/(g $\bar{m}$), using p = 4,000 Pa, g = 8.87 m s^{-2} and a mean molecular mass from 96.5% CO_2 and 3.5% N_2. The result is 6.25×10^{27} molecules m^{-2}. With the adopted 500 nm differential Raman cross section, the approximate expression 4π(dσ/dΩ) × 0.965N gives 0.00120. An angularly correct scattering law and cloud transport are needed before this quantity can predict an observed spectrum.

One Rayleigh corresponds to $10^{10}/(4\pi)$ photons m^{-2} sr^{-1} s^{-1}. Multiplication by hc/λ gives the integrated radiance at a chosen wavelength. At 500 nm the result is 3.16×10^{-10} W m^{-2} sr^{-1}. Division by an assumed 100 nm emission width is a hypothetical distribution of that energy, not an observed airglow band.

The remaining scale calculations use τ_Thomson = N_eσ_T, a thermal CO_2 backscatter scale $2\sqrt{kT/m}$, and a single-pass liquid Raman probability βL for small βL. Their inputs and values are listed in physical_scale_calculations.csv. Each is an order-of-magnitude physical check with stated assumptions. None supplies an absolute fluorescence calibration.

A guide to the complete numerical record

The calculation attachment preserves the existing analysis directory structure so that saved results can be traced to their scripts. The report's new tables and plots are collected in venus_long_report/. The prior CFHT, Jupiter, alternative-model and reconstruction work is in venus_three/previous/analysis/. The compact independent-instrument record is in venus_three/data_and_code/. The summary reconstruction inputs are in venus_summary/.

Table C1. Main numerical sources included in the attachment. Paths are relative to the attachment root. Full inventories and SHA-256 hashes are supplied separately.

Directory	Principal contents
venus_long_report/tables	Instrument comparison; all 22 named neighborhoods; physical estimates; worked reconstruction; depth examples
venus_long_report/figures	All report figures, plus the instrument-sample comparison supplied for enlargement
venus_long_report/chapters and code	Editable report text; document builder; figure and table calculation scripts
venus_three/previous/analysis/venus_line_check	CFHT pilot fits, line catalog, reference tests, raw-level and injection checks
venus_three/previous/analysis/venus_followup	Denser CFHT scans, Jupiter, color correlations and geometric matching
venus_three/previous/analysis/venus_mechanisms	Raman templates, broad wings, sky-fibre audit and physical estimates
venus_three/previous/analysis/venus_reconstruction	Individual reconstruction windows and continuum inputs
venus_three/previous/analysis/venus_manuscript	Reviewed sixteen-exposure shapes, source figures, references and earlier manuscript
venus_three/data_and_code/espresso	Individual and coadded fits, Vesta controls, extracted spectra, sensitivity tests and provenance
venus_three/data_and_code/uves	Raw-reduction recipes and calibration records, extracted arrays, row fits and BLUE merge diagnostics
venus_three/data_and_code/stis	Extracted detector-row spectra, masks, published-profile fits, background and injection tests
venus_three/data_and_code/shared and audit	Solar atlases and cross-checks used by the independent analyses
venus_summary/figure_inputs	Absorption samples, borrowed continuum, Vesta template and reconstruction inputs

The attachment contains the retained extracted numerical inputs, fit tables, figures and code. It does not duplicate every large original archive FITS file or distribute the ESO pipeline binaries. Archive identifiers, source URLs, calibration lists and available hashes identify those files. Repeating a raw reduction requires downloading the listed originals and installing the recorded pipeline environment. Rebuilding the report tables and the illustrated arithmetic can be done from the included compact record.

Some early scripts contain the original workspace paths. The attachment README identifies the corresponding portable working directories and explains which calculations use retained arrays and which retrieve external files. The new compilation scripts resolve their paths relative to the attachment root. Earlier prose and plots are preserved as history; where they disagree with this report, the corrections stated here take precedence. In particular, preliminary STIS atlas values, the ESPRESSO A–B variability claim, a negligible violet endpoint and an asserted chlorophyll-b width match are not current results.

Acknowledgments and use of AI

The observers, observatories and archive teams who obtained and preserved these public spectra are acknowledged. The work uses CFHT/ESPaDOnS data from the Canadian Astronomy Data Centre, ESO ESPRESSO and UVES observations, Hubble/STIS data from MAST, the IAG solar atlases, TSIS-1 solar irradiance and the cited Venus reflectivity products. The supplied 2026 absorption workbook was used with its published model interpretation.

The Astra model in ChatGPT was used to assist with archive searches, code preparation, spectral calculations, literature checks, figure preparation, drafting and revision. This assistance is acknowledged here; the model is not listed as an author. The record is supplied for independent checking, and the use of AI does not constitute outside scientific review.

References

Baker, A. D.; Blake, C. H.; Reiners, A. (2020). The IAG Solar Flux Atlas: Telluric Correction with a Semiempirical Model. The Astrophysical Journal Supplement Series 247, 24. doi:10.3847/1538-4365/ab6a1c.

Bartlett, J. S.; Voss, K. J.; Sathyendranath, S.; Vodacek, A. (1998). Raman scattering by pure water and seawater. Applied Optics 37, 3324. doi:10.1364/ao.37.003324.

Baumgardner, D.; Fisher, T.; Newton, R.; et al. (2022). Deducing the Composition of Venus Cloud Particles with the Autofluorescence Nephelometer (AFN). Aerospace 9, 492. doi:10.3390/aerospace9090492.

Brinkmann, R. T. (1968). Rotational Raman Scattering in Planetary Atmospheres. The Astrophysical Journal 154, 1087. doi:10.1086/149827.

Cochran, W. D.; Trafton, L.; Macy, W., Jr.; Woodman, J. H. (1981). Raman scattering in the Jovian atmosphere. The Astrophysical Journal 247, 734–740. doi:10.1086/159084.

Coddington, O. M.; Richard, E. C.; Harber, D.; et al. (2023). Version 2 of the TSIS-1 Hybrid Solar Reference Spectrum and Extension to the Full Spectrum. Earth and Space Science 10, e2022EA002637. doi:10.1029/2022ea002637.

Dixon, J. M.; Taniguchi, M.; Lindsey, J. S. (2005). PhotochemCAD 2: A Refined Program with Accompanying Spectral Databases for Photochemical Calculations. Photochemistry and Photobiology 81, 212-213. doi:10.1111/j.1751-1097.2005.tb01544.x.

Donati, J. F.; Semel, M.; Carter, B. D.; et al. (1997). Spectropolarimetric observations of active stars. Monthly Notices of the Royal Astronomical Society 291, 658-682. doi:10.1093/mnras/291.4.658.

Gaulme, P.; Schmider, F. X.; Gonçalves, I. (2018). Measuring planetary atmospheric dynamics with Doppler spectroscopy. Astronomy & Astrophysics 617, A41. doi:10.1051/0004-6361/201832868.

Gray, C. L.; Peter, K.; Pätzold, M.; et al. (2025). Venus' O 5577 Å Oxygen Green Line: A Global Diffuse Proton-Induced Aurora. Journal of Geophysical Research: Space Physics 130, e2024JA032851. doi:10.1029/2024ja032851.

Hu, C.; Voss, K. J. (1998). Measurement of solar-stimulated fluorescence in natural waters. Limnology and Oceanography 43, 1198-1206. doi:10.4319/lo.1998.43.6.1198.

Joiner, J.; Yoshida, Y.; Vasilkov, A. P.; et al. (2011). First observations of global and seasonal terrestrial chlorophyll fluorescence from space. Biogeosciences 8, 637-651. doi:10.5194/bg-8-637-2011.

Joiner, J.; Yoshida, Y.; Vasilkov, A. P.; et al. (2012). Filling-in of near-infrared solar lines by terrestrial fluorescence and other geophysical effects: simulations and space-based observations from SCIAMACHY and GOSAT. Atmospheric Measurement Techniques 5, 809-829. doi:10.5194/amt-5-809-2012.

Kleipool, Q.; Ludewig, A.; Babić, L.; et al. (2018). Pre-launch calibration results of the TROPOMI payload on-board the Sentinel-5 Precursor satellite. Atmospheric Measurement Techniques 11, 6439–6479. doi:10.5194/amt-11-6439-2018.

Köhler, P.; Behrenfeld, M. J.; Landgraf, J.; et al. (2020). Global Retrievals of Solar-Induced Chlorophyll Fluorescence at Red Wavelengths With TROPOMI. Geophysical Research Letters 47, e2020GL087541. doi:10.1029/2020gl087541.

Lee, Y. J.; García Muñoz, A.; Yamazaki, A.; et al. (2021). Investigation of UV Absorbers on Venus Using the 283 and 365 nm Phase Curves Obtained From Akatsuki. Geophysical Research Letters 48, e2020GL090577. doi:10.1029/2020gl090577.

Lee, Y. J.; García Muñoz, A.; Yamazaki, A.; et al. (2022). Reflectivity of Venus's Dayside Disk During the 2020 Observation Campaign: Outcomes and Future Perspectives. The Planetary Science Journal 3, 209. doi:10.3847/psj/ac84d1.

Lichtenthaler, H. K.; Schweiger, J. (1998). Cell wall bound ferulic acid, the major substance of the blue-green fluorescence emission of plants. Journal of Plant Physiology 152, 272-282. doi:10.1016/s0176-1617(98)80142-9.

Machado, P.; Widemann, T.; Peralta, J.; et al. (2021). Venus Atmospheric Dynamics at Two Altitudes: Akatsuki and Venus Express Cloud Tracking, Ground-Based Doppler Observations and Comparison with Modelling. Atmosphere 12, 506. doi:10.3390/atmos12040506.

Mogul, R.; Limaye, S. S.; Lee, Y. J.; Pasillas, M. (2021). Potential for Phototrophy in Venus' Clouds. Astrobiology 21, 1237-1249. doi:10.1089/ast.2021.0032.

Oklopčić, A.; Hirata, C. M.; Heng, K. (2016). Raman scattering by molecular hydrogen and nitrogen in exoplanetary atmospheres. The Astrophysical Journal 832, 30. doi:10.3847/0004-637x/832/1/30.

Penney, C. M.; St. Peters, R. L.; Lapp, M. (1974). Absolute rotational Raman cross sections for N_2, O_2, and CO_2. Journal of the Optical Society of America 64, 712. doi:10.1364/josa.64.000712.

Reiners, A.; Mrotzek, N.; Lemke, U.; et al. (2016). The IAG solar flux atlas: Accurate wavelengths and absolute convective blueshift in standard solar spectra. Astronomy & Astrophysics 587, A65. doi:10.1051/0004-6361/201527530.

Rossi, L.; Stam, D. M. (2018). Circular polarization signals of cloudy (exo)planets. Astronomy & Astrophysics 616, A117. doi:10.1051/0004-6361/201832619.

Sanghavi, S.; Frankenberg, C.; Nelson, R. R.; O'Dell, C. W.; Rosenberg, R.; Joiner, J. (2025). Impact of Raman Scattering on SIF Retrievals From Hyperspectral Satellite Observations. Geophysical Research Letters 52, e2024GL112777. doi:10.1029/2024GL112777.

Sato, T. M.; Satoh, T.; Sagawa, H.; et al. (2020). Dayside cloud top structure of Venus retrieved from Akatsuki IR2 observations. Icarus 345, 113682. doi:10.1016/j.icarus.2020.113682.

Slanger, T. G.; Cosby, P. C.; Huestis, D. L.; Bida, T. A. (2001). Discovery of the Atomic Oxygen Green Line in the Venus Night Airglow. Science 291, 463-465. doi:10.1126/science.291.5503.463.

Spacek, J.; Rimmer, P.; Owens, G. E.; et al. (2024). Production and Reactions of Organic Molecules in Clouds of Venus. ACS Earth and Space Chemistry 8, 89-98. doi:10.1021/acsearthspacechem.3c00261.

Spacek, J.; Rimmer, P. B.; Petkowski, J. J.; Lee, Y. J. (2026). A Model of UV–Blue Absorbance in Bulk Liquid of Venusian Cloud Aerosols Is Consistent with Efficient Organic Absorbers at High Concentrations. Astrobiology 26, 727-739. doi:10.1177/15311074261477502.

Sparks, W. B.; Hough, J.; Germer, T. A.; et al. (2009). Detection of circular polarization in light scattered from photosynthetic microbes. Proceedings of the National Academy of Sciences 106, 7816–7821. doi:10.1073/pnas.0810215106.

Taniguchi, M.; Lindsey, J. S. (2021). Absorption and Fluorescence Spectral Database of Chlorophylls and Analogues. Photochemistry and Photobiology 97, 136-165. doi:10.1111/php.13319.

Wolanin, A.; Rozanov, V. V.; Noël, S.; et al. (2015). Global retrieval of marine and terrestrial chlorophyll fluorescence at its red peak using hyperspectral top of atmosphere radiance measurements: Feasibility study and first results. Remote Sensing of Environment 166, 243--261. doi:10.1016/j.rse.2015.05.018.

Archive and instrument documentation

Canadian Astronomy Data Centre, CFHT archive.

ESO Science Archive Facility: programs 1102.C-0744(C) and 2101.C-5020(A).

MAST archive: Hubble program 12433.

STIS Instrument Handbook and calibration documentation.

TROPOMI calibrated Level 1B radiance bands.